Spin-crossover materials: Getting the most from x-ray crystallography

Sébastien Pillet

Spin crossover materials : getting the most from X-ray crystallography

Sébastien Pillet[a]

[a] Université de Lorraine, CNRS, CRM2, UMR 7036, Nancy, 54000, France

ABSTRACT

The physical phenomenon of spin crossover in molecular crystals is a multiscale process whose properties rely on the supramolecular organization of the spin crossover active elements, their interactions within the crystal packing and their dynamics. The delicate balance between short-range and long-range structural reorganization upon the spin transition is at the origin of remarkable and fascinating physical phenomena such as thermal, light induced and pressure induced hysteresis, multi-step transitions and multimetastablility. A complete understanding of the various phenomena associated to spin crossover requires a comprehensive and thorough characterization of the overall structural architecture at all scales which goes beyond the average static crystal structure. This tutorial surveys the practical use of X-ray crystallography notably in non-ambient conditions to provide a direct view of the physical processes operating in spin crossover molecular solids from bulk single crystals to nano-crystalline powder. Advanced X-ray crystallography methods are reviewed and illustrated with a series of model examples.

I. INTRODUCTION

In the most general situation in condensed matter, the physical or chemical properties of a given material are intimately connected to its structural organization (i.e. atomic arrangement) and structural dynamics. As a consequence, the prerequisite to any understanding, design and property improvement of those material is the comprehensive determination of its structure in all its spatial and temporal aspects.

The spin crossover (SCO) phenomenon relates to the switching between two spin states, the high spin (HS) state and the low spin (LS) state in transition metal ions by a change of temperature, or application of pressure, light, magnetic field.[1–3] Since the early studies of SCO materials, crystal structure determination in connection with thermo-magnetic, photo-magnetic and optical spectroscopic characterizations has become an indispensable analytical tool developing a deep physical understanding of the various processes related to the molecular spin state change. Knowledge about molecular and supramolecular structural organization and bonding derived from conventional X-ray

structural crystallography and accumulated from numerous synthesized SCO materials allows taking advantage of structure-properties relationship[4–7] following crystal engineering strategies for the design of new systems with almost predictable properties. For all synthesized SCO materials, conventional structural X-ray crystallography allows to decipher their spin crossover properties revealed by thermomagnetic measurements. The precise change of molecular structural conformation upon the HS to LS spin state change (change of coordination bond distances, and octahedron distortion) is systematically quantified. Structural determination under light or pressure has been developed in order to uncover the structural response to external perturbations as well. Different and specific transition behaviors or transition dynamics have been related to different supramolecular organization in SCO polymorphs[8,9] or multistable states.[10] The origin of two-step (and later multi-step) transitions has been traced back to symmetry breaking transitions and formation of ordered HS-LS patterns[11], while more exotic mechanisms, such as spin transition connected to a reversible bond breaking[12] could not have been interpreted without a clear picture of the corresponding structural changes. For all these reasons, conventional X-ray crystallography appears therefore as an unavoidable experimental mean providing a microscopic point of view in connection with macroscopic magnetic or optical spectroscopy studies.

The structural organization of a typical SCO molecular crystalline solid consists of several components : (i) a SCO active coordination entity built from a central d^4-d^7 transition metal ion surrounded by several coordinating ligands, (ii) counter ions and (iii) lattice solvent molecules. The equilibrium structural configuration of the SCO solid relies on a combination of local energetic contributions (electron pairing energy, energy splitting between the e_g and t_{2g} orbitals), molecular structural configuration, short range intermolecular interactions (hydrogen bonds, van der waals interactions, π-π stacking) and long range interactions mediated by elastic forces. The whole physical processes associated to SCO molecular solids are closely related to the entire structural organization, and its response to a change of thermodynamic parameters (temperature and pressure) or upon application of external constraints (stress, light, magnetic field). A spin crossover crystalline solid may also be pictured as a continuous elastic medium in which HS-LS switching molecules can be considered as point elastic defects.[13,14] As such, the HS-LS molecular deformation upon spin state switching is considered as an elastic dipole, which interacts strongly with the entire elastic medium. The exact instantaneous relaxed conformation corresponds to the minimum of elastic energy of the entire solid. It is conveniently considered that these interactions between the switching molecules, called phenomenologically cooperativity, control most of the solid-state SCO phenomena. Strong elastic interactions result in abrupt first order spin transitions, associated with thermal hysteresis, and remarkable instabilities in the light-induced spin transition regime. Optical microscopy measurements

performed in various thermal and optical excitation conditions[15–19,19–21] have clearly shown the major importance played by the development of structural and spin state domains upon all these processes. Altogether, the SCO process occurs on several spatial scales from the microscopic molecular level to the mesoscopic scale. A detailed comprehensive understanding of the whole structural architecture requires to develop appropriate structural models and associated experimental approaches, using advance X-ray crystallography methods.

There has already been a number of reviewing reports in the literature dealing with the various aspects of the structural properties of SCO materials.[22–25] In the present tutorial, we adopt a different and complementary perspective, by considering the structural information one can derive directly from reciprocal space. Our main objective is to discuss how far X-ray scattering methods can provide a detailed description of the structural organization going beyond the well-established and conventional structure determination. We restrict ourselves to static, quasi-static and kinetic structural description on purpose, excluding fast and ultrafast dynamic processes, which have been reviewed recently in an exhaustive manner.[25] In addition, although a few neutron scattering[26,27] and electron diffraction[28,29] experiments, which are very complementary to X-ray scattering techniques, have been carried out on SCO materials, we do not consider these approaches in the present tutorial. The outline is the following. In section II, we introduce basic crystallography concepts and the X-ray scattering formalism which is applicable to any SCO materials (amorphous, microcrystalline powder or single crystal). Section III deals with the derivation of structural features beyond the average picture. Section IV focusses on the development of long-range ordered commensurate and incommensurate superstructures, while heterogeneous phase transitions and mesoscopic domain nucleation and growth are discussed in section V. The last section addresses the manipulation of the structure through external stimuli, like temperature or light-irradiation. Some emerging perspectives, such as the use of the pair distribution function are anticipated in the conclusion.

II. X-RAY SCATTERING FOR AMORPHOUS, NANOCRYSTALLINE, POLYCRISTALLINE AND SINGLE CRYSTAL SPIN CROSSOVER SOLIDS

SCO molecular materials have been designed and elaborated over the years in various forms such as single crystals, microcrystalline powders, nanoparticles, or even nanocomposites. Well appropriate methods and instruments have to be chosen in order to derive relevant information on the structural organization of such quite complex and various materials. X-rays scattering methods are very much suitable for that purpose for several reasons : (i) the short X-ray wavelength (nearly 1 Å and below) is compatible with interatomic distances allowing a high spatial resolution to be achieved, (ii) X-rays

present high penetration depth in matter, (iii) X-ray diffractometers with various environment conditions (temperature, pressure, under light illumination) are readily available in most crystallographic laboratories while synchrotron radiation facilities offer possibilities for more specific experiments.

In the most general formalism, when an incident X-ray beam interacts with a complex system built from a large collection of N_{at} atoms, whether it is amorphous, a small cluster, or a crystalline solid, the scattered intensity (Thomson elastic scattering) for scattering vector $\boldsymbol{Q}$ $\left(\boldsymbol{Q} = \boldsymbol{k_i} - \boldsymbol{k_f}\right)$ is given in electron units by:

$$I(\boldsymbol{Q}) = \sum_{j,k}^{N_{at}} f_j(Q) f_k(Q) e^{i\boldsymbol{Q}\cdot[\boldsymbol{r_j}-\boldsymbol{r_k}]} \quad (1)$$

where $f_j(Q)$ (noted in short f_j) is the scattering factor of atom *j* located at position $\boldsymbol{r_j}$, $\boldsymbol{r_j} - \boldsymbol{r_k}$ is the interatomic vector between atoms *j* and *k*.

Equation (1) shows that the scattered intensity contains all the structural information in the form of pairwise interatomic vectors $\boldsymbol{r_j} - \boldsymbol{r_k}$. The goal of any structural determination and analysis is to extract relevant parameters (atomic positions, atomic displacement parameters) from the scattered intensity.

A. Total X-ray scattering for amorphous and nanocrystalline SCO solids : the pair distribution function approach

Deriving the structural organization on an atomic scale of amorphous or nanocrystalline SCO materials for which the structural coherence extends only over a few nanometers is a challenging task. Conventional crystallographic structure solution approaches rely on X-ray diffraction of periodic single crystal or microcrystalline powders. These approaches are no longer appropriate for amorphous systems (or badly crystallized powder) or nanocrystals for which strict long-range periodicity is not fulfilled, while local atomic ordering may still be present. The corresponding X-ray scattering pattern is characterized by broad not well-resolved peaks and high diffuse background. This is the case for instance for the triazole-based coordination polymer family of general formula $[(\text{R-trz})_3\text{Fe}]X_2$ (R-trz = triazole derivative, X = monovalent counter-anion). In such cases, total X-ray scattering and modelling of the pair distribution function (PDF) can be an attractive alternative strategy.[30] The PDF ($G(r)$, defined in equation 4) is a real space quantity, which gives the probability of finding any atom at a distance r from another atom. It may be simply seen as a radial distribution of all the interatomic distances r_{jk} in the considered sample. The PDF can be derived from a careful treatment of total X-ray scattering experiments using high energy X-rays (typically E > 20 KeV) corresponding to short wavelength (λ < 0.6 Å) with good statistics and angular resolution, available at synchrotron radiation

facilities. Structural information is obtained in a second step by fitting a structural model to the experimentally derived PDF.

For amorphous materials, or a nanocrystalline powder, assuming isotropic spatial probability in space, equation (1) can be simply written as :

$$I(Q) = \sum_{j,k}^{N_{at}} f_j f_k \frac{\sin Qr_{jk}}{Qr_{jk}} \quad (2)$$

which is called the Debye scattering equation. Q is the magnitude of the scattering vector (also known as the momentum transfer), $Q = |\boldsymbol{Q}| = 4\pi sin\theta/\lambda$, where θ is half the scattering angle 2θ,and λ is the X-ray radiation wavelength.

The structure function $S(Q)$ is derived from the coherent total scattered intensity $I(Q)$ after proper correction for background and other experimental effects, and normalization :

$$S(Q) = 1 + \frac{I(Q) - \sum_j c_j |f_j(Q)|^2}{|\sum_j c_j f_j(Q)|^2} \quad (3)$$

where c_j is the concentration of atom type j in the sample.

The sine Fourier transform of the normalized and reduced total coherent scattered intensity $S(Q)$ leads to the pair distribution function (r) :

$$G(r) = \frac{2}{\pi}\int_0^\infty Q[S(Q) - 1]\, sin(Qr) dQ \quad (4)$$

This function describes the radial distribution of all atomic pairs in the probed sample, and as such contains all the information on the structural organization.

An example in the case of the poorly crystallized SCO coordination polymer $[Fe(Htrz)_2(trz)].(BF_4)$ is illustrated in figure 1. The total X-ray scattering pattern contains only a few distinguishable peaks at low angle (low Q range) and does not extend far in reciprocal space so that a conventional Rietveld structural refinement is not realistically feasible. Sine Fourier transform of the measured total scattered intensity $I(Q)$ yields the experimental PDF $G(r)$, which consists of well resolved features. The first four PDF peaks correspond to interatomic distances of short range origin (C-C, C-N, Fe-N contributions), while the peak at r = 7.3 Å is related to the Fe…Fe second neighbor distance, and considered as a signature of the 1D chain structure. Peaks at higher r values result from all the long-range intra-chain and inter-chain atomic pairwise contributions.

Modelling of the PDF can be carried out either (i) in reciprocal space, by fitting a prior structural model and calculating the corresponding scattered intensity using the Debye equation (equ. 2), or in direct space by fitting the structural model to the experimentally derived PDF (equ. 4).

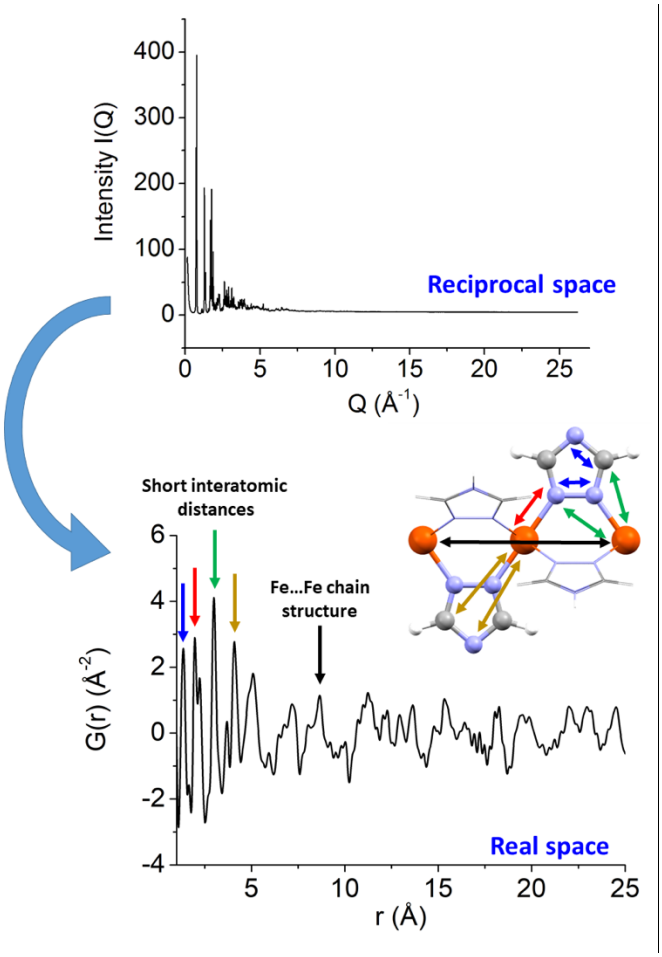

FIG. 1. The PDF analysis uses high energy total X-ray scattering (total coherent scattered intensity $I(Q)$) to reveal all interatomic distances in the measured sample. The experimental data have been measured on the MS beamline at the Swiss Light Source using an X-ray energy of E = 30 keV (λ = 0.43 Å) up to a maximum resolution of Q_{max} = 26 Å^{-1}. The main contributions to the PDF are depicted as colored arrows, corresponding to the interatomic distances highlighted in the structural scheme.

B. Single crystal X-ray scattering of spin crossover solids

The scattered intensity described in its most general formulation in equation 1 is valid for any measurable sample. A single crystal is defined by the fundamental property of lattice periodicity. Its structure may be simply built from a reference unit cell containing n atoms at position $\boldsymbol{r}_{j0}$. Each unit cell of the crystal is located at a lattice vector $\boldsymbol{r}_N$, so that each atom of the crystal is located at a position $\boldsymbol{r}_j = \boldsymbol{r}_N + \boldsymbol{r}_{j0}$.

For a periodic SCO solid, the scattered intensity factorizes into the product of two terms :

$$I(\boldsymbol{Q}) = \sum_{j,k}^{N_{at}} f_j f_k e^{i\boldsymbol{Q}\cdot[\boldsymbol{r}_j - \boldsymbol{r}_k]} = \overbrace{\sum_{N,N'} e^{i\boldsymbol{Q}\cdot[\boldsymbol{r}_N - \boldsymbol{r}_{N'}]}}^{Lattice\ sum} \times \overbrace{\sum_{j,k}^{n} f_j f_k e^{i\boldsymbol{Q}\cdot[\boldsymbol{r}_{j0} - \boldsymbol{r}_{k0}]}}^{Unit\ cell\ scattered\ intensity} \quad (5)$$

where the sum runs over the lattice sites (N and N') and the atoms of the reference unit cell (j,k).

The scattered intensity $I(\boldsymbol{Q})$ is simply related to the product of the unit cell structure factor $F(\boldsymbol{Q})$ and the interference function $\Gamma(\boldsymbol{Q})$. The former describes the chemical nature and position $\boldsymbol{r}_{j0}$ of the atoms in the reference unit cell of the crystal, while the interference function characterizes the periodicity of the SCO crystal.

$$I(\boldsymbol{Q}) = \Gamma(\boldsymbol{Q})\Gamma^*(\boldsymbol{Q}) \times F(\boldsymbol{Q})F^*(\boldsymbol{Q}) \quad (* \text{ is the complex conjugate}) \quad (6)$$

With $\Gamma(\boldsymbol{Q}) = \sum_N e^{i\boldsymbol{Q}\cdot\boldsymbol{r}_N}$ and $F(\boldsymbol{Q}) = \sum_j^n f_j e^{i\boldsymbol{Q}\cdot\boldsymbol{r}_{j0}}$ (7)

$\Gamma(\boldsymbol{Q})$ is a periodic oscillating function which takes maximum values at integer coordinates of the reciprocal space vector $\boldsymbol{Q} = 2\pi(h\boldsymbol{a}^* + k\boldsymbol{b}^* + l\boldsymbol{c}^*)$, where $\boldsymbol{a}^*$, $\boldsymbol{b}^*$ and $\boldsymbol{c}^*$ are the reciprocal lattice vectors. $F(\boldsymbol{Q})$ is the unit cell structure factor, a complex quantity which is the sum of the scattering contributions at $\boldsymbol{Q}$ of all the atoms of the reference unit cell.

Figure 2 shows the real space crystal packing of the SCO compound [Fe(bapbpy)$(NCS)_2$] (space group *C2/c*) projected along the crystallographic axis $\boldsymbol{b}$, and the corresponding calculated X-ray scattering pattern using a simulated crystal of 10*1*10 unit cells. The perfect periodicity of the crystal packing in direct space is mirrored by the ordered pattern of the diffraction peaks in reciprocal space. As a matter of fact, strong peaks are observed for integer values of the reciprocal space coordinates h and l. In addition, the *C2/c* space group imposes some conditions on the observable diffraction peaks. The *C* cell centering and *c* mirror plane (perpendicular to the $\boldsymbol{b}$ axis) lead to the systematic absence (hkl) with h+k=2n+1, and (h0l) with l=2n+1 respectively. The limited size of the simulated crystal (10*1*10 unit cells) is revealed by noticeable oscillations in the [h00] and [00l] directions around each Bragg peak (see Fig. 2d).

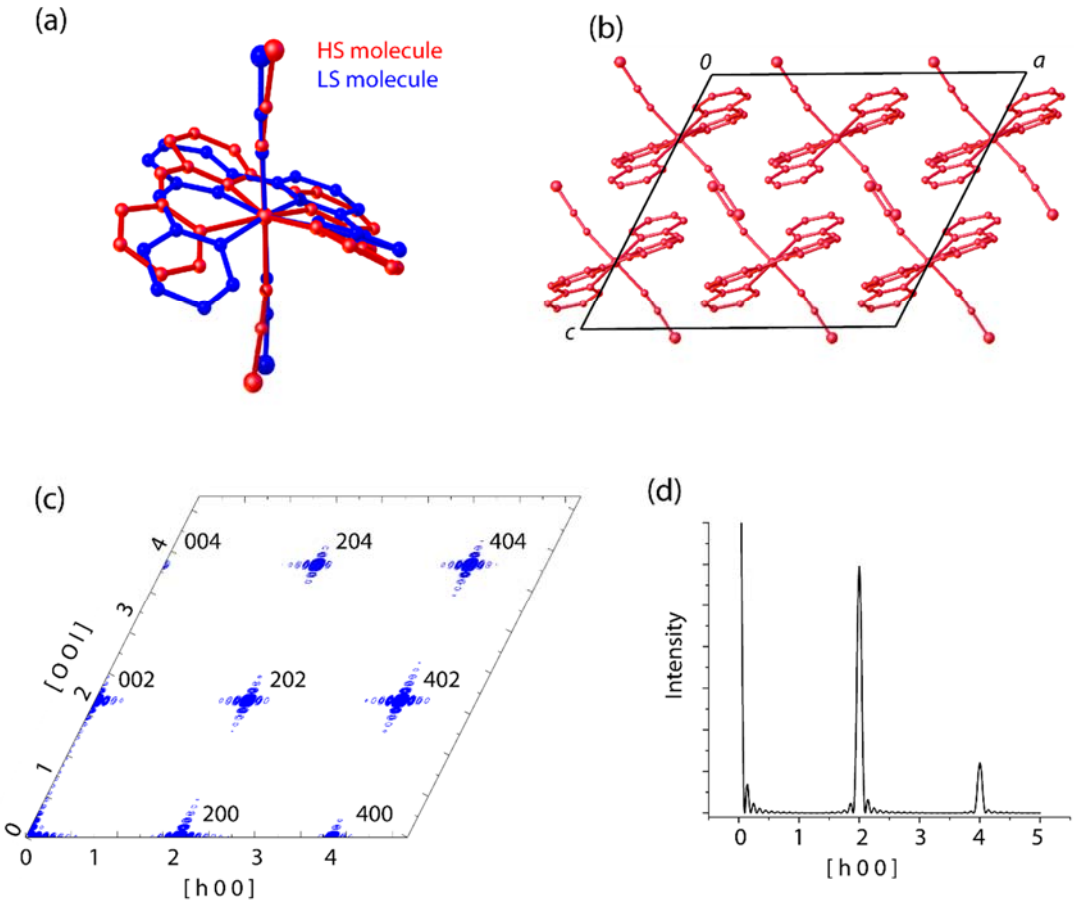

Fig. 2. (a) Superposition of the HS (in red) and LS (in blue) molecular structure of the SCO compound [Fe(bapbpy)$(NCS)_2$]. (b) Projection of the crystal packing of the HS state in the *C2/c* space group. (c) Calculated scattering pattern in the (h0l) layer of reciprocal space. (d) Intensity profile along the [h00] row.

It is well known that upon a HS to LS SCO, the crystal structure exhibits strong modifications which reflects in reciprocal space as variation in Bragg peak position and Bragg peak intensity. First of all, the unit cell distorts in size and shape, which correlates to relative changes of the reciprocal lattice vectors $\boldsymbol{a}^*$, $\boldsymbol{b}^*$ and $\boldsymbol{c}^*$, so that the diffraction peaks located at $\boldsymbol{Q} = 2\pi(h\boldsymbol{a}^* + k\boldsymbol{b}^* + l\boldsymbol{c}^*)$ in reciprocal space significantly shift in position. This peak displacement quantifies the amplitude and anisotropy of the HS to LS unit cell deformation. This is further characterized by a modification of the interference function $I(\boldsymbol{Q})$. In addition, the HS to LS atomic displacements in the unit cell induce a modification of the structure factor $F(\boldsymbol{Q})$ for each Bragg reflection (hkl) by a quantity ΔF_{hkl}. This modification of the structure factors upon switching the spin state is illustrated in figure 3 in the form of an Argand diagram. Fig. 3a illustrates the construction of the structure factor F_{hkl}^{HS} as a summation of four atomic contributions $f_{1\ldots4}$. Owing to the structural reorganization, and mostly the Fe-N bond shortening, both the structure factor amplitude $|F_{hkl}|$ and phase φ_{hkl} are changed from F_{hkl}^{HS} to F_{hkl}^{LS} (Fig. 3b).

The structural reorganization upon the HS to LS transition can thus be quantified by monitoring the Bragg peak intensity variation.

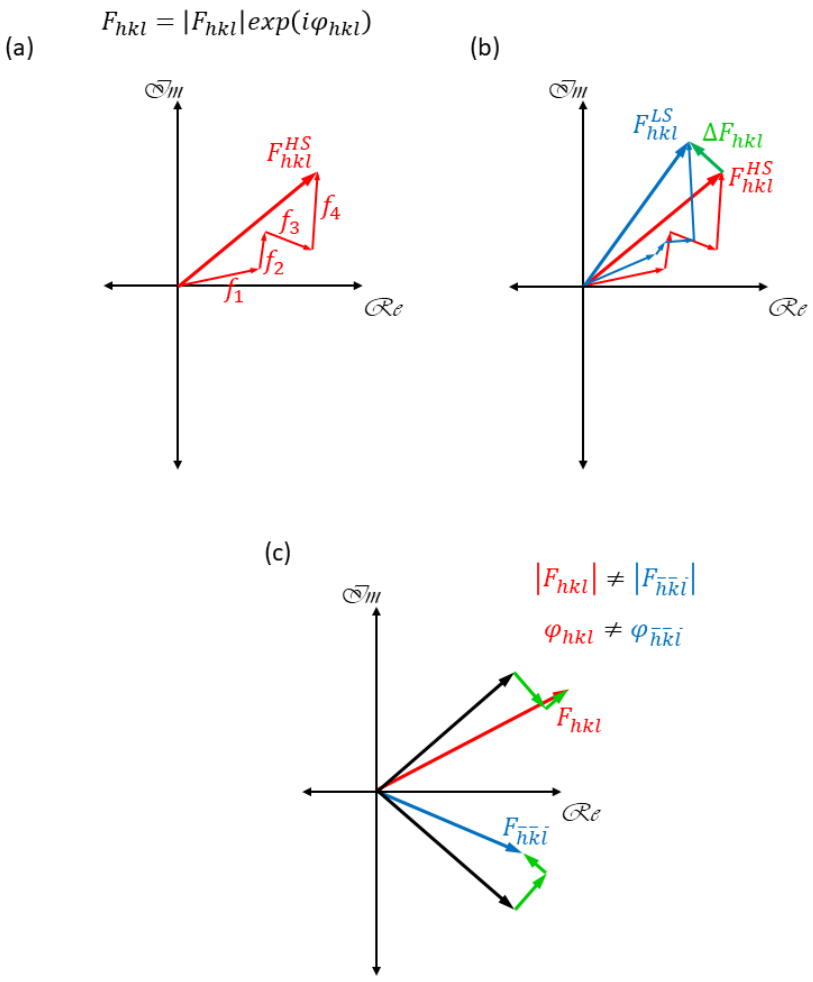

Fig. 3. (a) Scheme of a HS structure factor F_{hkl}^{HS} in the form of an Argand diagram in the complex plane. The structure factor, which is a complex quantity defined by its modulus $|F_{hkl}|$ and phase φ_{hkl}, consists in a summation of the atomic contributions f_j according to equation 7. (b) Superposition of the HS and LS structure factors, highlighting the structural contrast between HS and LS configurations. ΔF_{hkl}, depicted as a green arrow, is the HS-LS difference in structure factor. (c) Argand diagram in the case of non-negligible anomalous dispersion effects. Black arrows correspond to the structure factors of so-called Friedel pairs F_{hkl} and $F_{\bar{h}\bar{k}\bar{l}}$ in the absence of anomalous dispersion, while red and blue arrows include significant $f'(\hbar\omega)$ and $f"(\hbar\omega)$ anomalous dispersion contributions (see section III.D).

C. X-ray diffraction of microcrystalline spin crossover powder

A SCO microcrystalline powder sample consists of an enormous number of very small crystals having completely random orientation. In such a case, the scattering process is still described by the single crystal equation (5), albeit considering reduced crystallite size. For a fixed position of the powder sample, only some crystallites have the correct orientation to be in a scattering position for a given family of (hkl) plane. Rotating continuously the sample while measuring the scattered intensity provides a collection of measurable scattering cones of half apex angle $2\theta_{hkl}$. There is a cone of diffracted signal for each spacing d_{hkl}. A typical X-ray diffraction powder pattern consists in a continuous distribution of intensity along the scattering angle 2θ, which is deconvoluted in individual (quite often overlapped) diffraction profiles located at each $2\theta_{hkl}$ and analyzed in a structural Rietveld refinement.

For a small parallelepiped crystal of reduced size N_a, N_b, N_c in the three crystallographic directions; equation (6) writes:

$$I(\boldsymbol{Q}) = F(\boldsymbol{Q})F^*(\boldsymbol{Q}) \times \frac{sin^2(\pi N_a \boldsymbol{Q}\cdot\boldsymbol{a})}{sin^2(\pi \boldsymbol{Q}\cdot\boldsymbol{a})} \times \frac{sin^2(\pi N_b \boldsymbol{Q}\cdot\boldsymbol{b})}{sin^2(\pi \boldsymbol{Q}\cdot\boldsymbol{b})} \times \frac{sin^2(\pi N_c \boldsymbol{Q}\cdot\boldsymbol{c})}{sin^2(\pi \boldsymbol{Q}\cdot\boldsymbol{c})} \quad (8)$$

For very small crystallites, N_a, N_b, N_c are small ; the three corresponding quotients broaden the peak profile on the powder X-ray diffraction pattern : this is called particle size broadening.

Considering a powder sample of small cubic crystals ($N_a = N_b = N_c = N$) in perfect random orientation, and approximating the three quotients of equ (8) by identical Gaussian functions (same maximum ordinate and same area), the full width in radians at half maximum of a diffraction peak profile is approximated by the Scherrer equation:

$$W(2\theta) = \frac{K\lambda}{Lcos\theta} \quad (9)$$

where K is a dimensionless crystallite shape factor (K~0.94) and L is the mean size of the ordered crystalline domains.

According to its simple use, the Scherrer equation is conveniently used for deriving the approximate coherent structural domain size in microcrystalline powder or nanoparticles of SCO, but it should be stressed that the particle size L entering equation (9) is the volume of a coherent structural domain in a particle, and should not be confused with the particle size itself which could be imaged through scanning electron microscopy (SEM). The Scherrer equation provides a very rough approximation of the particle size broadening, and does not account for the broadening resulting from structural strain effects. More elaborated profile analysis have been proposed for a more appropriate size-strain and instrumental broadening (slit width, wavelength dispersion, superposition of $K_{\alpha 1}$ and $K_{\alpha 2}$ lines) deconvolution.

For SCO molecular materials, the crystal structure is usually of low symmetry (triclinic or monoclinic space group most of the time), so that the corresponding powder X-ray diffraction pattern displays strong peak profile overlap. It is nevertheless very informative on the structural transition mechanism, microstructure development, and structural coherence aspects as will be discussed in the following sections.

D. Experimental methods

Extracting physically relevant information from an X-ray diffraction experiment requires appropriate experimental conditions, and a correct choice of the diffraction instrument. Conventional X-ray diffractometers are readily available in many laboratories with various characteristics, while more challenging and unusual experiments can be carried out using synchrotron radiation facilities.

Laboratory diffractometers are running with X-ray tubes, allowing selecting between different fixed X-ray energies corresponding to different X-ray radiation wavelengths (Cu K-α radiation $E_{Cu} = 8.05\ keV$, $\lambda_{Cu} = 1.54$ Å ; Mo K-α radiation $E_{Mo} = 17.48\ keV$, $\lambda_{Mo} = 0.71$ Å; Ag K-α radiation $E_{Ag} = 22.16\ keV$, $\lambda_{Ag} = 0.56$ Å). Short wavelength means that a high maximum scattering angle 2θ can be reached (a high maximum scattering vector Q) leading to accurate derived structural parameters such as atomic positions or atomic displacements parameters. On the contrary, the scattered intensity $I(\boldsymbol{Q})$ is proportional to the third power of the X-ray radiation wavelength, so that choosing a short wavelength results in weak scattering.

Synchrotron radiation facilities offers several advantages with respect to X-ray tubes based laboratory diffractometers for structural determination and analysis. At first, the incoming X-ray flux is several orders of magnitude higher, which renders weak scattering signals (for instance surstructure reflections, or weak diffuse scattering signals) detectable. Secondly, the X-ray radiation energy is continuously tunable, so that a specific X-ray wavelength can be adjusted for different purposes. Tuning the wavelength close to the absorption edge of a specific chemical element of a studied sample could for instance be used to enhance anomalous dispersion effects or enhance the scattering contrast for that given element. Thirdly, use can be made of the time and spatial coherence properties of synchrotron radiation X-rays to perform various imaging experiments (X-ray diffraction imaging, phase contrast imaging) or X-ray photon correlation spectroscopy to study structural details with a high spatial resolution or to study structural dynamics. Finally, synchrotron radiation beamlines are equipped with efficient optics which allow focusing the incoming beam down to micrometer or sub-micrometer size; high spatial resolution can be achieved for mapping the structural inhomogeneities

of a sample. Alternatively, the intrinsic time structure of the synchrotron X-ray beam can be used for challenging time resolved experiments ; this is out of the scope of the present tutorial.

Pair distribution function analyses are conducted using typical powder diffraction instruments under total scattering conditions with very short X-ray radiation wavelength. The scattered signal consists of weak diffuse scattering contributions so that a high intensity X-ray beam, achievable at synchrotron radiation facilities, is mandatory, although preliminary acceptable measurements for sample quality evaluation purposes can be conducted using a laboratory diffractometer with Mo or Ag X-ray tube. Reliable data are typically measured over a wide range of momentum transfer up to a high Q_{max} desirable value of > 30 $Å^{-1}$. Dedicated beamlines have been optimized for this kind of measurements at the Advanced Photon Source, or at Diamonds, and appropriate measurements can be conducted at most of high energy (E > 45 keV) crystallography beamlines at third generation synchrotron facilities. The data processing requires several corrections for instrumental effects (air scattering and scattering from the sample holder subtraction, multiple and Compton scattering correction, absorption correction) and normalization steps, which are fairly routinely accounted for.

Very relevant for the understanding of the photophysical properties of SCO materials is the evaluation of the structural reorganization upon light excitation. Such analysis is carried out using a specific X-ray diffraction setup adapted with an in situ excitation device; this is called photocrystallography.[31–36] The usual experimental method for photocrystallography requires selecting and adapting an appropriate excitation source with well-adjusted characteristics (type of excitation source, coherence of the excitation source, excitation wavelength, excitation power). The type of light source can be either a laser (coherent monochromatic source) or more conveniently a LED (incoherent source). LEDs offer the advantage of being very cheap, with a wide range of available wavelength, at the expense of a poor but acceptable monochromaticity. Most of the current photocrystallographic experiments use monochromatic X-ray radiation sources, while the polychromatic Laue diffraction methods make use of a broad energy range of the X-ray beam, which results in a faster data collection.[37] This is a convenient strategy for very sensitive samples.

III. REAL STRUCTURAL ORGANIZATION OF SPIN CROSSOVER SYSTEMS BEYOND THE AVERAGE STRUCTURE

Standard single crystal structure determination aims at deriving the positions of the atoms in the reference unit cell of the crystal and interatomic connectivity, assuming a perfect lattice periodicity. The main assumption relies on the perfect structural equivalence between all the unit cells of the crystal. For SCO materials, it routinely consists in collecting X-ray diffraction data at a given

temperature corresponding to a given spin state, chosen according to the thermomagnetic behavior, followed by structure solution and refinement of the structural model. The outcome of such an experiment is the spatial and time average of the atomic configuration in the probed sample. In a similar way, structure determination of microcrystalline powder uses the so-called Rietveld refinement in order to refine the atomic positions, and possibly the atomic displacement parameters for good quality powder X-ray diffraction data. Although these routine approaches may be relevant in assessing the average structural organization, very important additional structural properties and characteristics going beyond the average structure may prove crucial in understanding exact SCO processes. The purpose of this section is to present and discuss how far detailed structural information can be obtained from inspection, analysis and modelling of the X-ray diffraction pattern, covering from single crystal, to microcrystalline powder and even non well-ordered materials.

A. The local structure from the pair distribution function analysis

There has been recently a huge interest in the development and the physical characterization of SCO nanoparticles[38–40] and nanocomposites[41], while the structural determination of such nanoscale objects is far from being trivial. The PDF approach, only recently applied to SCO materials, is an appropriate strategy, which does not require any periodical organization of the sample, contrary to X-ray diffraction approaches. A seminal PDF work has been pioneered by Grosjean et al. in order to evaluate the structural organization in the SCO material $[Fe(Htrz)_2(trz)].(BF_4)$. [42]

As an illustrative example, figure 4 presents the PDF of the $[Fe(Htrz)_2(trz)].(BF_4)$ compound determined by total X-ray scattering experiments performed on the MS beamline at the Swiss Light Source synchrotron as a function of temperature (E = 30 keV, $Q_{max} = 26\text{Å}^{-1}$) for a nanocrystalline powder sample in a Kapton capillary. This compound exhibits a strongly cooperative thermal spin transition centered at nearly 360K with a 40K thermal hysteresis. Below 340K, $[Fe(Htrz)_2(trz)].(BF_4)$ is in the LS state, while raising the temperature above 380K induces a complete LS to HS transition. Figure 4 shows the high contrast in the PDF as a function of the Fe^{II} spin state. As discussed in paragraph 2.A, the first four PDF peaks correspond mostly to the Fe coordination environment, and interatomic distances within the triazole ligand. Peaks in the high r range originate from the chain structure and supramolecular inter-chain packing. As shown in figure 4c, the first peak, corresponding to C-C and C-N bond distances is insensitive to the Fe^{II} spin state. On the contrary, the other three peaks exhibit a displacement to larger distances upon the LS to HS transition, signature of the Fe-N bond elongation. In parallel, the Fe…Fe peaks at higher r values (for instance around 15.5 Å) shifts to higher values owing to the elongation of the polymeric $[Fe(Htrz)_2(trz)]$ infinite chain.

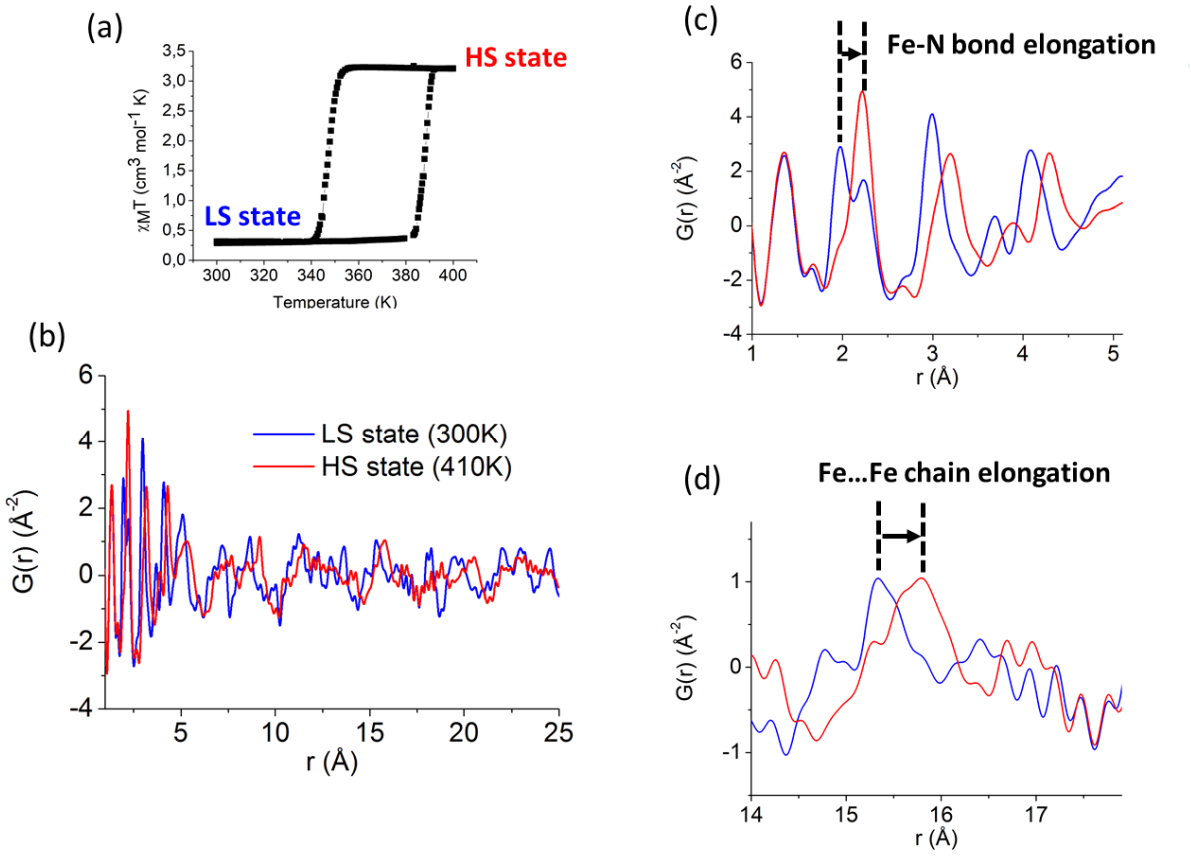

FIG. 4. (a) Spin transition properties of the $[Fe(Htrz)_2(trz)].(BF_4)$ compound in the form of the molar magnetic susceptibility as a function of temperature. (b-d) PDF derived at 300K in the LS state (in blue), and at 410K in the HS state (in red).

From the present example, it is seen that the PDF analysis is well appropriate to characterize the local and long-range order structure in not well crystalized or nanoparticles of SCO materials owing to the large structural reorganization upon the LS to HS transition. In the case of $[(R\text{-}trz)_3Fe]X_2$ compounds, the PDF provides (i) the local coordination structure, (ii) a proof of the formation of 1D chains and (iii) inter-chain supramolecular organization. This is a very attractive approach complementary to X-ray absorption techniques (EXAFS and XANES)[43,44] and transmission electron microscopy (TEM).[29] The former gives only a structural description of the close proximity of the central metal atom (Fe^{II}), while TEM is hardly applicable to high resolution owing to a frequent propensity to degradation of the sample under the focused electron beam. The major limitation of the PDF analysis in the context of the structural characterization of SCO materials is that the derived structural picture is spherically averaged in space, all directional (or anisotropic) considerations are obviously lost. It may be foreseen that the PDF approach is only emerging in SCO, and will find future applications for studying defect structures or short-range ordering.

B. Deciphering spin state spatial distribution from the Bragg intensity

Correlations of the distribution of HS and LS states in a SCO crystal play a key role in all the transition processes, and manifest themselves in the thermal transition curves or decay curves of the light-induced metastable HS state.[45] Correlations result from the short-range interactions between the SCO molecules competing with long-range interactions of elastic origin. Mapping the distribution of HS and LS states with a molecular resolution, is a challenging task. As discussed in section II, the X-ray scattered intensity from a single crystal results from wave interferences and is modulated by the pairwise interatomic vectors $\boldsymbol{r}_{jk}$. Owing to the large molecular structural reorganization, the integrated Bragg intensities therefore contain significant information on that distribution.

The single crystal structure is described by the unit cell structure factor given in equation (7), whose structural parameters are the scattering factor f_j (describing the atomic chemical type) and position $\boldsymbol{r}_{j0}$ of each atom in the unit cell. This corresponds to an ideal perfectly periodic and ordered picture of the crystal structure, averaged over space and time. Subtle differences may emerge in the Bragg intensities depending on the real spatial distribution of the atoms in the 3D crystal. Consider for instance two extreme situations of a SCO crystal containing 90% of HS molecules and 10% of LS molecules.

In the first case, the HS/LS molecules are randomly distributed (labelled RD) in the crystal. Accordingly, each atomic site in the average unit cell can be approximated by a weighted superposition of the HS and LS configuration, and the corresponding approximated structure factor is given by:

$$F_{RD}(\boldsymbol{Q}) = \; p_{HS}\sum_j^n f_j^{HS} e^{i\boldsymbol{Q}\cdot\boldsymbol{r}_{j0}^{HS}} + p_{LS}\sum_j^n f_j^{LS} e^{i\boldsymbol{Q}\cdot\boldsymbol{r}_{j0}^{LS}} = p_{HS}\times F^{HS}(\boldsymbol{Q}) + (1-p_{HS})\times F^{LS}(\boldsymbol{Q}) \quad (10)$$

The scattered intensity is finally proportional to :

$$F_{RD}^2(\boldsymbol{Q}) = \; (p_{HS})^2\times|F^{HS}(\boldsymbol{Q})|^2 + (1-p_{HS})^2\times|F^{LS}(\boldsymbol{Q})|^2 + p_{HS}(1-p_{HS})[F^{HS}(\boldsymbol{Q})\times F^{LS}(\boldsymbol{Q})^* + F^{LS}(\boldsymbol{Q})\times F^{HS}(\boldsymbol{Q})^*] \quad (11)$$

In a second hypothesis, the LS molecules in the SCO crystal can be clusterized in one or several LS domains (as could be observed in a first order spin transition with hysteresis). In this cluster model situation (labelled CM), the scattered intensity is proportional to :

$$F_{CM}^2(\boldsymbol{Q}) = \; (p_{HS})^2\times|F^{HS}(\boldsymbol{Q})|^2 + (1-p_{HS})^2\times|F^{LS}(\boldsymbol{Q})|^2 \quad (12)$$

Comparing equation (11) and (12) reveals that the scattered intensity in a single crystal diffraction experiment of a SCO compound can provide interesting indications on the spatial distribution of the

HS and LS species in the crystal. Vorontsov and Coppens have quantified this intensity difference in the case of a photoexcited molecular crystal.[46]

For SCO materials, by monitoring the evolution of the intensity of Bragg reflections along a thermal spin transition, or during a LS to HS photoexcitation or HS to LS relaxation could provide detailed information on the spatial distribution of the HS/LS molecular species.

C. Spin crossover coupled to structural disorder

In general, the crystal structure of SCO solids presents intricate architectures built from spin-active molecular complexes and spin-inactive counterparts, such as solvents or counter-ions. Quite frequently, some fragments of the architecture present a structural disorder, and may undergo complete or partial ordering triggering (or triggered by) the HS-LS transition. Disorder can therefore be considered as an order parameter of the spin transition,[47] which can affect the whole spin transition processes in several ways. From a thermodynamic perspective, a structural disorder may modulate the energy gap between the LS and HS states, as discussed for instance for the SCO compound $[Fe(DAPP)(abpt)](ClO_4)_2$ for which a disorder of the DAPP ligand and the perchlorate anion couples to the spin state change.[48,49] Solvent disorder has the capability to modify the characteristics of a spin transition, shift the transition temperature, strengthen or weaken the cooperativity (affecting the hysteresis), while long range ordering may trigger the onset of a superstructure, and generate a two-step transition phenomenon, such as observed for the solvated $[Fe^{II}(2\text{-picolylamine})_3]$ family of compounds. [11,50]

Structural disorder manifests itself in a conventional structural refinement by abnormally elongated thermal ellipsoids. Models of disorder can be derived from a structural refinement against single-crystal diffraction data, providing the position of the atoms in the several disorder conformations, as well as the occupancy of each conformation. The structure factor formalism is very similar to those expressed in equation (10), assuming a random spatial distribution of the conformations in the single crystal without any short-range correlations between disordered molecules:

$$F_{disorder}(\boldsymbol{Q}) = \; p_{config.A} \sum_j^n f_j^A e^{i\boldsymbol{Q}\cdot\boldsymbol{r}_{j0}^A} + p_{config.B} \sum_j^n f_j^B e^{i\boldsymbol{Q}\cdot\boldsymbol{r}_{j0}^B} \qquad (13)$$

for a two configurations structural model (config. A and config. B), with respective populations $p_{config.A}$ and $p_{config.B}$.

The corresponding conformational entropy can be calculated in terms of Shannon entropy considering the different thermally accessible conformation states as :

$$S = -k_B \sum p_j ln(p_j) \quad (14)$$

Structural disorder can affect the kinetics of the spin state switching processes, leading in some cases to a decoupling between the structural transition and the spin transition. The spin-crossover compound $[Fe(n\text{-}Bu\text{-}im)_3(tren)](PF_6)_2$ may be considered as an example. It shows quite complex thermal and light-induced SCO processes, whose kinetics result from the structural rearrangement of the butyl chains of the various ligands on several conformations.[51] Detailed single-crystal diffraction measurements have been carried out as a function of time in different situations. Figure 5 illustrates the relationship between the HS to LS relaxation and the conformation of the two butyl chains (noted A and B) quantified through X-ray crystallography (formally, $p_{chain.A}$ and $p_{chain.B}$ are two refined parameters of the structural model corresponding to the ordering of the two butyl chains). The different regimes in the HS to LS relaxation originates from the progressive rearrangement and complete ordering of the two butyl chains.

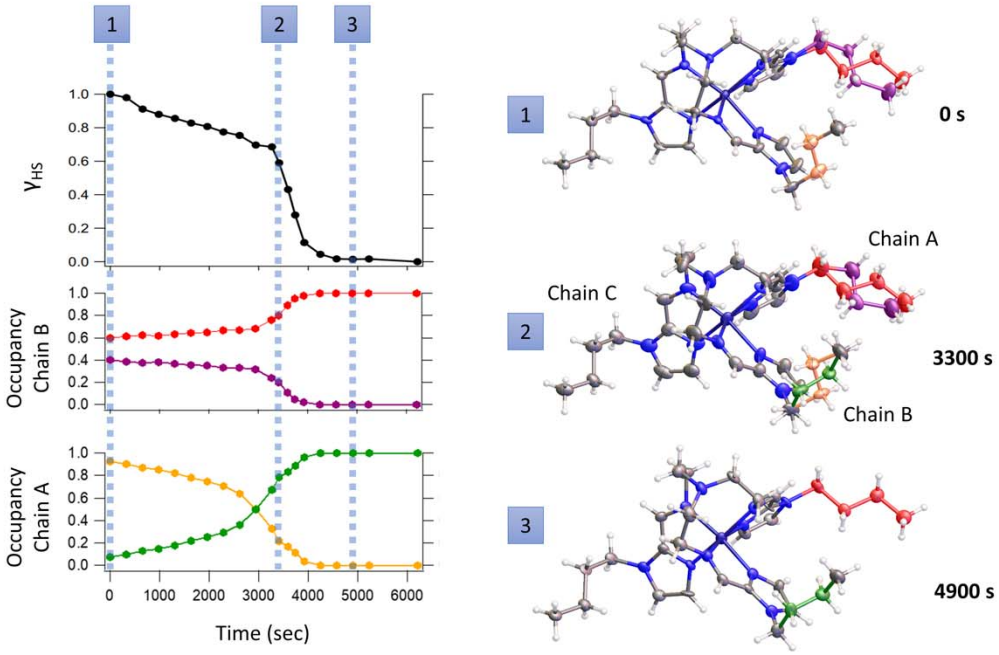

FIG. 5. Relationship between the HS to LS relaxation curve and the evolution of the butyl chains conformations after irradiation at 90K from the LS state of $[Fe(n\text{-}Bu\text{-}im)_3(tren)](PF_6)_2$. Reprinted with permission from Delgado *et al*. J. Am. Chem. Soc. **140**, 12870 (2018). Copyright 2018 American Chemical Society.

The precise characterization of the disorder as a function of external (e.g. light excitation) or thermodynamic parameters (T, P) is therefore of prime importance, and readily reachable from X-ray crystallography. If the disorder is not completely random, but consists in short range correlations between the disorder conformations, the X-ray diffraction pattern exhibits characteristic diffuse

scattering; the structural modeling discussed above is not sufficient, and more elaborated models of the structural correlations have to be accounted for in a specific 3D pair distribution function analysis for instance. Such a handling has not been developed yet in the SCO community.

D. Deciphering chirality from X-ray Bragg intensities

A high challenge in crystal engineering and molecular design of SCO materials is to control in a rational way the elaboration of chiral SCO materials. The chirality functionality, if interrelated to the SCO behavior, offers remarkable potential properties and applications such as electro-optic effects, non-linear optical properties, chiroptical switching, magneto-optic properties, spin filtering or spin polarization in molecular spintronics.[52,53] The chiral functionality may emerge from different possibilities : use of chiral ligands (such as macrocyclic ligands with asymmetric substituents) in a mononuclear complex,[54] use of chelating ligands which twist around the metal center (such as for the [Fe(phen)$_3$] complex),[52,53,55] confining SCO molecules in chiral host framework,[56] or co-crystalizing SCO molecules with chiral counterions.[57] Chiral SCO materials of different architectures have been reported in the literature: chiral SCO metal-organic frameworks,[58] chiral SCO mononuclear complexes[52–55,57], chiral SCO polymeric chains.[59] Synthesis with equimolar racemic composition of the two enantiomers usually pack in a centrosymmetric space group, or crystallize as inversion twins. In interesting cases, one may observe a complete spontaneous resolution of the different Δ and Λ enantiomers during crystallization. Each crystal can be further distinguished by single-crystal circular dichroism measurements.

Single crystal X-ray diffraction has the potential to distinguish between different enantiomers and resolve the absolute structure in the following way. In the general case, Friedel pair reflections F_{hkl} and $F_{\overline{h}\overline{k}\overline{l}}$ do not differ in amplitude ($|F_{hkl}| = |F_{\overline{h}\overline{k}\overline{l}}|$), while their phase is opposite ($\varphi_{hkl} = -\varphi_{\overline{h}\overline{k}\overline{l}}$). Their intensity is therefore identical

$$I_{hkl} = I_{hkl} I^*_{hkl} \times F_{hkl} F^*_{hkl} = I_{\overline{h}\overline{k}\overline{l}} I^*_{\overline{h}\overline{k}\overline{l}} \times F_{\overline{h}\overline{k}\overline{l}} F^*_{\overline{h}\overline{k}\overline{l}} = I_{\overline{h}\overline{k}\overline{l}} \quad (15)$$

The X-ray diffraction pattern is in this case centrosymmetric. This situation corresponds to the black arrows in figure 3c.

Contrary to this, if the wavelength of the X-ray beam is tuned close to an absorption edge of at least one heavy element of the measured crystal (Fe in the case of SCO complexes), resonant scattering effects lead to an energy dependent correction of the atomic scattering factor $\left(f_{Fe}(Q, \hbar\omega) = f^0_{Fe}(Q) + f'(\hbar\omega) + if''(\hbar\omega)\right)$. As a consequence, the intensity of Friedel pairs become subtly

different, and as such can be distinguished in high accuracy X-ray diffraction data measurements. This corresponds to the blue and red arrows in figure 3c.

In order to tackle the chirality problem in X-ray crystallography, it is mandatory to choose the appropriate X-ray wavelength (or energy) at which the values of the anomalous dispersion coefficients $f'(\hbar\omega)$ and $f"(\hbar\omega)$ are high, that is to say an energy close to the absorption edge of one of the heaviest element of the crystal. Iron K-edge occurs at 7.11 keV. For iron SCO compounds, the anomalous dispersion coefficients are enhanced at Cu-Kα radiation ($f' = -1.14\text{e}$ and $f'' = 3.12\text{e}$) and to a lower extent at Mo-Kα radiation ($f' = 0.34\text{e}$ and $f'' = 0.84\text{e}$). A copper X-ray tube is therefore an appropriate choice for absolute structure determination with a laboratory diffractometer, while synchrotron radiation offers a perfect energy tunability to optimize the anomalous dispersion effects. Absolute structures are detected in the structural refinement procedure following the approach formulated by Flack, which consists simply in considering the single crystal as built from the two opposite handed structural domains (twinning by inversion) and refining the domain ratio, called the Flack parameter.[60] When the Flack parameter is close to zero, the material is enantiopure and the atomic coordinates derived from the refinement present absolute (fixed handedness) structural configuration. Absolute structures can also be detected in the distribution of Bragg intensities following the approach of Simon Parsons.[61,62]

E. Electron density distribution from high-resolution X-ray diffraction

The fundamental interaction between incident X-rays and a single crystal sample consist of elastic coherent scattering (Thomson scattering) with the electron density distribution $\rho(\boldsymbol{r})$ of the sample. In a traditional structural determination and analysis from X-ray diffraction on a single crystal, one assumes in a first approximation that the total electron density distribution is a superposition of spherically averaged atomic contributions neglecting any deformation of the electron density owing to interatomic and intermolecular interactions. This is called the independent atom model (IAM model). Measuring X-ray diffraction data with exceptionally good accuracy and very high angle resolution (at least up to $Q = 15\text{Å}^{-1}$) allows going beyond the IAM approximation, by detecting and modelling the deformation of the atomic electron density distribution. For that purpose, the Hansen-Coppens multipolar model[63] considers the atomic electron density as resulting from three contributions : the fixed spherical electron density of the core electrons, the spherical contribution from the valence electrons, and the aspherical contribution from the valence electrons developed on a spherical harmonic basis.

$$\rho_{atomic}(\boldsymbol{r}) = \rho_{core}(r) + \rho_{valence}(r) + \delta\rho_{valence}(\boldsymbol{r}) \quad (15)$$

Such an approach is traditionally used to investigate the bonding situation in ground state crystalline systems, and has been applied in a few cases to the metastable states of SCO materials.[64,65]

At first, the electron density multipolar model allows a better deconvolution of thermal smearing effects than for the IAM model. As a consequence, the derived structural parameters (bond distances and atomic displacement parameters) are much more accurate, and the hydrogen atoms better localized. The experimentally modelled electron density distribution allows also analyzing various chemical bonding features relevant to SCO processes, such as the electronic distribution within the 3d orbitals of the central metal ion, in line with its electronic configuration. It offers also the possibility of calculating related properties analytically from the total electron density : the electrostatic potential (for selected molecular or atomic fragments for instance) or the crystal interaction energy.

IV. FROM SHORT-RANGE CORRELATIONS TO LONG-RANGE ORDERING OF MOLECULAR SPIN STATES

There have been some manifestations in the thermomagnetic and photomagnetic curves that short-range and long-range correlations and fluctuations of the distribution of molecular spin states play a major role in solid state SCO processes. The most obvious situation consists in multi-step transitions associated to the ordering of HS/LS molecules in an ordered pattern on well-defined plateaus. Magnetic relaxation curves after photo-excitation exhibits in some cases long relaxation tails (stretched exponentials or stretched sigmoidal curves) which require accounting for long-range interactions in addition to the mean-field self-accelerated relaxation process to be described properly.[66,67] There is therefore an absolute need for the determination and analysis of the structural component of short-range and long-range ordering. We have seen in section III.B that the intensity of Bragg peaks in single crystal diffraction contains some information on the spatial distribution of spin states, we discuss in the present section the development of specific spin state pattern.

By definition, a perfect single crystal is composed of identical unit cells stacked on a regular three-dimensional lattice. This situation is illustrated in figure 6a where the red dots correspond to HS molecules, and the green square represents the unit cell of the crystal. The X-ray diffraction pattern of such a three-dimension crystal is a three-dimension array of points (Bragg peaks) regularly spaced, reflecting the perfect periodicity (illustrated for instance in Fig. 2). Suppose the atoms (or molecules) of the unit cells are subjected to longitudinal (Fig. 6b) or transverse (Fig. 6c) displacements whose amplitudes vary sinusoidally in space with wavevector $\boldsymbol{q} = \frac{\boldsymbol{a}^*}{2}$. The spin state distribution can also be modulated with the same wavevector. The unit cell of the modulated crystal is in that case doubled in the direction of the modulation propagation; the corresponding X-ray diffraction pattern exhibits

additional sharp satellite reflections, which reflects the onset of a new periodicity in the crystal. The amplitude of the modulation is the order parameter of the phase transition, so that the intensity of the satellite reflections operates as a measure of the modulation amplitude, and as such of the order parameter of the transition. This situation occurs for two-step transitions with a long-range ordered [HS-LS] pattern for instance, such as in the SCO compound $[Fe(2\text{-pic})_3]Cl_2.EtOH$.[11] In a more general case, depending on the value of the modulation wavevector, the unit cell expands by a simple multiple to map the crystal onto itself. In this commensurate modulated phase, the atoms in different unit cells are displaced by the same distance. In case (d), the modulation wavevector is not commensurable with the underlying crystal lattice ($\boldsymbol{q} = 0.62 \times \boldsymbol{a}^*$) so that no two atoms are displaced by the same distance with respect to their position in the undistorted crystal. The unit cell is not changed, and it is impossible to find any lattice vector which maps the crystal onto itself. The crystal symmetry does not belong to the 230 possible space groups in three dimensions. However, the crystal is still perfectly ordered (although not periodic in 3D) in the sense that the displacive modulation is described by an analytical function, which is itself periodic in an additional fourth dimension. The symmetry operations act in a 3D+1 superspace for a single modulation; the fourth dimension refers to the phase of the modulation. Incommensurate spatially modulated structures have been reported in a limited number of SCO materials, taking place either during the thermal transition or the photoinduced transition.[68–72]

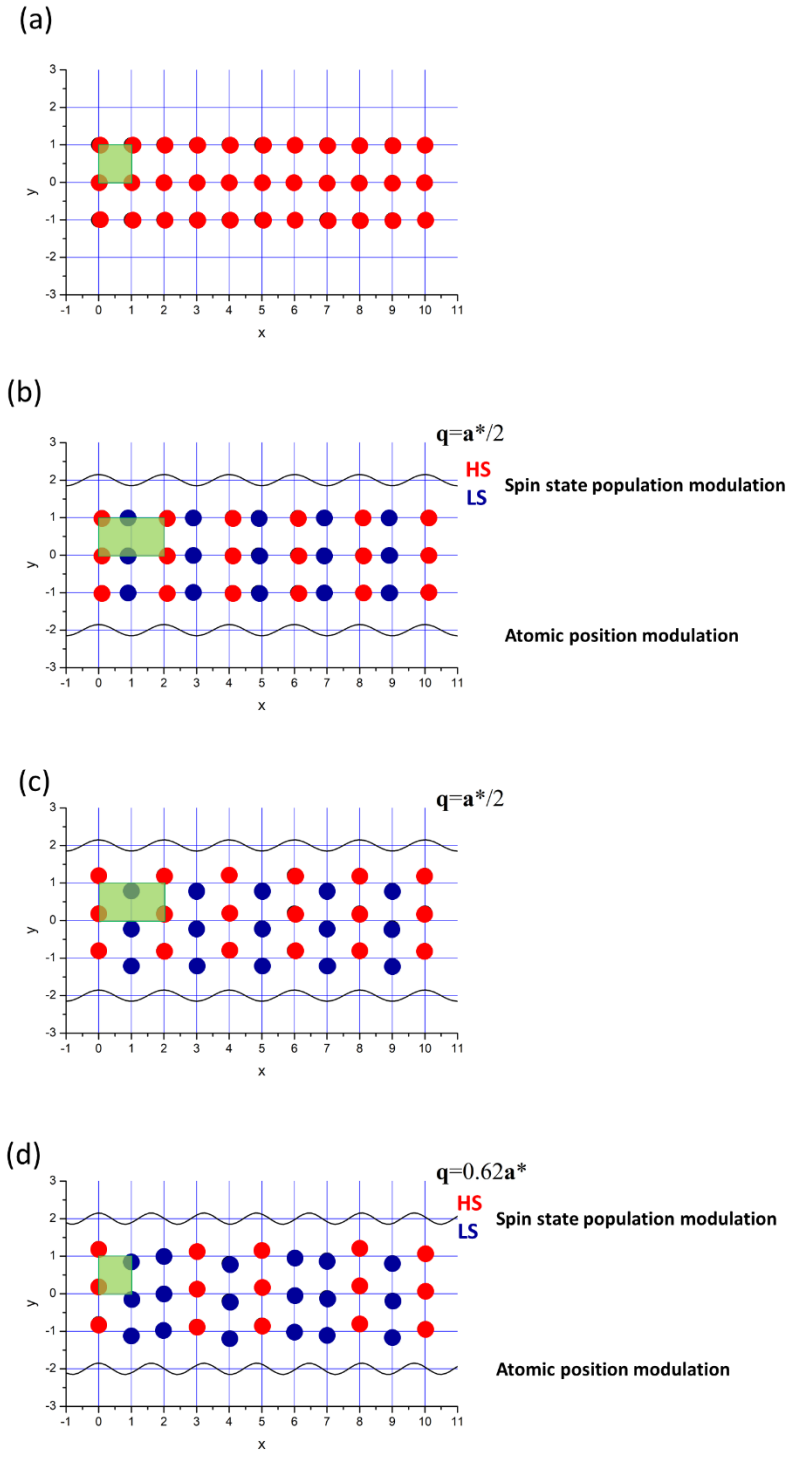

FIG. 6. (a) A regular two-dimensional crystal containing HS molecules (red dots). The unit cell is represented by a green square. (b) A commensurate longitudinal displacive modulation of wavevector $\boldsymbol{q} = \frac{\boldsymbol{a}^*}{2}$ correlated to a HS/LS distribution (HS in red, LS in blue). The unit cell is doubled along the propagation direction. (c) A commensurate transverse displacive modulation. (d) An incommensurate

transverse displacive modulation of wavevector $\boldsymbol{q} = 0.62 \times \boldsymbol{a}^*$ correlated to an incommensurate modulation of HS/LS distribution with the same wavevector.

A. Short-range ordering characterized from diffuse X-ray scattering

X-ray diffraction from a perfect periodic single crystal is characterized by sharp Bragg peaks, plus satellite reflections in the case of long-range ordered modulations. Bragg peaks scattering reflects the mean electron density distribution in the unit cells of the crystal. In a real crystal, the electron density may vary from one unit cell to another under the effect of disorder, the development of short-range modulations, the formation of nanodomains, or crystal phonons. If the local variation of electron density from adjacent unit cells is correlated, X-ray diffuse scattering emerges, reflecting the short-range collective atomic or molecular behavior. If the electron density is separated into two components, the average periodic unit cell electron density $\overline{\rho(\boldsymbol{r})}$ and the weakly correlated deviations from periodic $(\boldsymbol{r})$:

$$\rho(\boldsymbol{r}) = \overline{\rho(\boldsymbol{r})} + \delta(\boldsymbol{r}) \quad (16)$$

then the scattered intensity can be approximated by :

$$I(\boldsymbol{Q}) \approx I_{Bragg}(\boldsymbol{Q}) + I_{Diffuse}(\boldsymbol{Q}) \quad (17)$$

X-ray diffuse scattering has been observed for instance at the two-step spin transition for the polymeric SCO compound [Fe(bdpp)$(NCSe)_2$] with a chain structural topology.[73] The structurally similar compound [Fe(bdpp)$(NCS)_2$] presents a two-step transition with two distinct Fe^{II} centers and a transition sequence Fe1(HS)-Fe2(HS) -> Fe1(HS)-Fe2(LS) -> Fe1(LS)-Fe2(LS) with an ordered spin state pattern in the intermediate phase. The two phase transitions are isomorphous without change of space group type (*P-1*). On the contrary, [Fe(bdpp)$(NCSe)_2$] adopts a crystal structure characterized by a single Fe^{II} site in the monoclinic space group *C2/c*, even in the intermediate phase, so that the HS and LS molecular species are spatially disordered on the same site in the unit cell if one describes the structure from the Bragg reflections only. The measured X-ray diffraction pattern displays additional weak diffuse scattering planes perpendicular to the crystallographic direction [101], indicating the onset of a 1D long range ordering of alternating HS/LS species along the polymeric chains, without correlations between the chains. The specific ordering in this compound manifests itself in the relaxation kinetics after light excitation at very low temperature. The kinetics follow a stretched exponential behavior with a Gaussian distribution of the apparent activation energy.

X-ray diffuse scattering has also been reported and analyzed for the archetypical SCO compound $[Fe(ptz)_6](BF_4)_2$, which presents an abrupt HS to LS spin transition whose structural properties depend on the cooling rate.[74] For a rapid cooling, the spin transition is isomorphous, with preservation of the high-symmetry rhombohedral *R-3* space group. Upon slow cooling (e.g. < 1K.min^{-1}) a LS disordered phase is formed. This process is thermally reversible. Similarly, a quick cooling to 100 K and monitoring of the single-crystal X-ray diffraction pattern shows a slow progressive structural transition from the ordered LS phase to the disordered LS phase, revealed by a broadening and a splitting of the diffraction peaks (Fig. 7). The dynamics of the phase transition has been interpreted using a structural model built from microdomains of identical perfect trigonal layers which are stacked by the rhombohedral centering vector $\left[\frac{1}{3}, -\frac{1}{3}, \frac{1}{3}\right]$ or the rhombohedral centering vector plus an additional shift $\left[\frac{1}{3}+\delta_x, -\frac{1}{3}+\delta_y, \frac{1}{3}\right]$. Optimization of the parameters of the model (correlation length along $\boldsymbol{c}^*$, shift amplitude between layers, composition in different layers) reproduces the experimental results adequately. The formation of such microdomains results from a symmetry reduction in the LS state : $[Fe(ptz)_6](BF_4)_2$ is a ferroelastic SCO compound as will be discussed in more details in a following section. The dynamics of microdomain formation impact severely the dynamics of the spin transition itself in this compound. The analysis of the Bragg peak splitting and broadening allowed modelling the short-range order that develops progressively in the LS state.

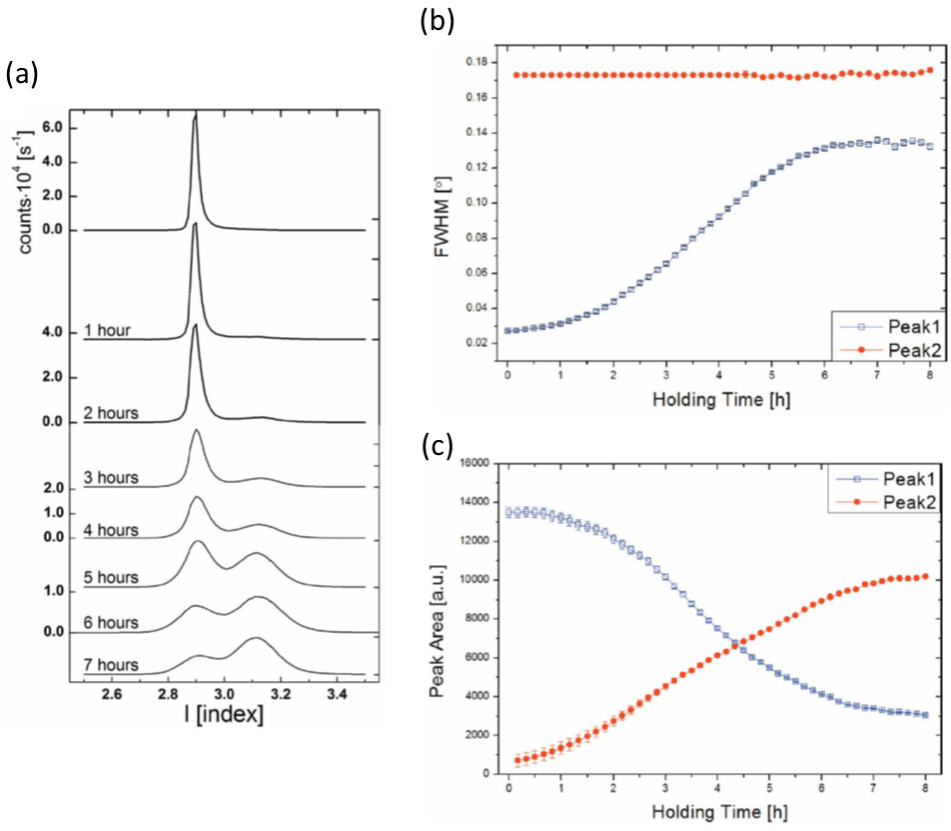

FIG. 7. (a) Time dependence of q-scans of the (113) Bragg reflection along the direction of $\boldsymbol{c}^*$ in isothermal condition after quick cooling to T = 100K for the SCO compound $[Fe(ptz)_6](BF_4)_2$. The slow Bragg peak broadening and splitting evidence the LS ordered to LS disordered phase transition. (b,c) Time dependence of the Full Width at Half Maximum of the two peaks, together with the peak area. Reproduced from Kusz *et al*. Acta Cryst. B **68**, 40 (2012) with permission of the International Union of Crystallography.

To summarize, these two examples show that advanced crystallographic measurements performed in appropriate temperature-time conditions provide detailed information on the dynamics of short-range correlations or formation of microdomains closely linked to the spin transition processes.

B. Periodic commensurate HS/LS pattern development

Although most of the thermally induced or light induced spin transitions reported in the literature undergo a single-step spin state switching, in some cases, SCO materials display fascinating collective self-ordering behaviors manifested in multi-step transitions, with or without hysteresis, and resulting in a wide variety of long-range ordered patterns of HS and LS molecules.[75–80,70] Up to now, spin state transitions with up to eight more or less clearly identified steps have been reported. In most of the cases, the crystal structure has been solved for all the steps, allowing a clear description of the HS/LS supramolecular ordering. Multistep transitions may result from molecular multistability, from the presence of crystallographically different metal sites, or from the subtle competition between antagonistic short-range and long-range interactions. We will concentrate hereafter on this specific latter case for which the transition is further associated to symmetry breaking phenomena, involving a change of space group type and/or translational symmetry during which the SCO active molecular entities may change their site symmetry and Wyckoff position. The phase transition is associated to concerted displacive atomic and molecular motions triggered by the change of HS-LS structural conformation (especially the HS to LS drastic coordination sphere contraction) during the SCO. The symmetry breaking phase transition originates from a strong coupling between the spin state switching and long-range interactions of elastic origin within the crystal lattice. It is described by at least two coupled order parameters, the totally symmetric average HS fraction γ_{HS}, and the symmetry breaking order parameter(s) η measuring the degree of long-range molecular spin state order.

From a mechanistic perspective, symmetry breaking transitions and the development of ordered patterns of HS/LS molecules has been described within the framework of the Landau theory governed

by the evolution of symmetry breaking order parameters,[81] or rationalized through microscopic elastic models. In the most simple HS/LS ordering, microscopic models considering two sublattices have been proposed, the symmetry breaking transition and HS/LS ordering originating from "ferroelastic" intrasublattice interactions and "antiferroelastic" inter-sublattices interactions.[82,83] For more exotic [HS-HS-LS-LS] or [HS-HS-LS] ordering patterns, more elaborated theories have been introduced.[84,85] Recently, elastic models relying on competing elastic interactions between the SCO active sites resulting from steric effects (called elastic frustration) in the crystal coupled to the HS/LS spin state switching emerged.[86,87]

The direct inspection of the diffraction pattern along a symmetry breaking transition can yield a lot of qualitative and quantitative information on the exact mechanism by which the transition proceeds, and on the ordered pattern of HS/LS molecules within the crystalline framework. The phase transition may be characterized by a shift of some Bragg peaks quantifying the distortion of the unit cell, splitting of Bragg peaks originating from a reduction of point group symmetry and formation of different ferroelastic domains with different domain states (discussed in section V.B), appearance of superstructure reflections due to a change of lattice periodicity.

The SCO compound $[Fe(bapbpy)_2(NCS)_2]$ is a good illustrative example of such self-organization in multi-step transition.[75,88] This compound, whose molecular structure has already been described above (Fig. 2a), exhibits a two-step thermal spin transition with hysteresis (the three phases are labelled phase I, II and III with temperature decrease). At room temperature (phase I), it crystalizes in the monoclinic *C2/c* space group with half a $[Fe(bapbpy)_2(NCS)_2]$ molecule in the asymmetric unit, the central Fe^{II} ion is located on a special position on the two-fold axis perpendicular to the crystallographic ***b*** axis. A projection of the HS crystal packing is given in figure 8a, as well as the corresponding experimental X-ray diffraction pattern.

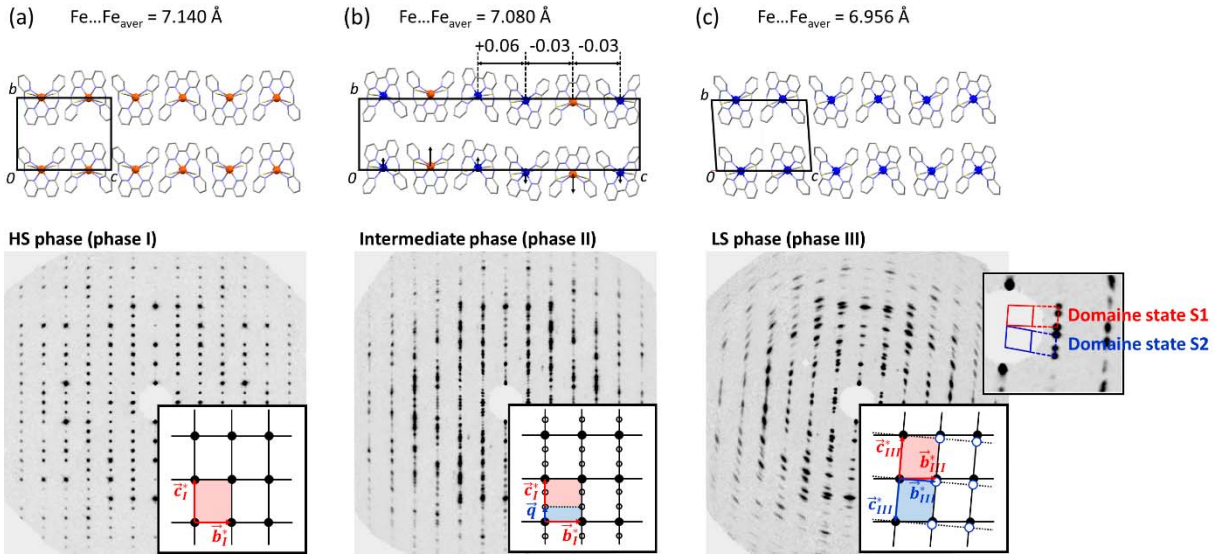

Fig. 8. (Top) Crystal packing of $[Fe(bapbpy)_2(NCS)_2]$ in phase I (a), phase II (b) and phase III (c). HS (viz. LS) molecular entities are depicted in red (viz. blue). Note the displacive and HS/LS ordering modulation in the intermediate phase. (Bottom) X-ray diffraction pattern of $[Fe(bapbpy)_2(NCS)_2]$ measured in the HS, intermediate and LS phases (reconstruction of the (0kl) layer). The indexing with the reciprocal lattice vectors is shown in the corresponding inset.

Upon cooling, $[Fe(bapbpy)_2(NCS)_2]$ undergoes a symmetry breaking transition at 235 K (from phase I to phase II), the corresponding diffraction pattern in the intermediate (phase II) shows the appearance of superstructure reflections along the reciprocal space vector $\boldsymbol{c}^*$. Those reflections can be indexed introducing a commensurate wave vector $\boldsymbol{q} = \frac{1}{3}\boldsymbol{c}^*$. This change in the X-ray diffraction pattern is the signature of the onset of a new periodicity in the single crystal, the unit cell is tripled in the direct space direction of $\boldsymbol{c}$ without change of space group type *C2/c*. The new unit cell becomes therefore $(\boldsymbol{a}, \boldsymbol{b}, 3\boldsymbol{c})$, while the asymmetric unit is changed with one complete LS molecule and half a HS molecule with change of Wyckoff position (site symmetry) for the Fe^{II} sites. Conceptually, the change of lattice periodicity corresponds to a change in the interference function $\Gamma(\boldsymbol{Q})$ introduced previously. In the intermediate phase, $\Gamma(\boldsymbol{Q})$ exhibits secondary maxima at positions $\left(h + \frac{1}{3}\right)\boldsymbol{c}^*$ and $\left(h + \frac{2}{3}\right)\boldsymbol{c}^*$ owing to the unit cell tripling in the direction of $\boldsymbol{c}$. The corresponding crystal structure is depicted in figure 8(b). In the symmetry broken phase (called the intermediate phase), the HS and LS molecules self-organize to form a long-range ordered pattern with the [HS-LS-LS] sequence. In addition, the molecules undergo a harmonic displacive modulation (transverse and longitudinal) with a periodicity of 42.39 Å, corresponding to the length of the $\boldsymbol{c}$ crystallographic axis. The transverse modulation is depicted as black arrows in figure 8b while the longitudinal modulation corresponds to alternate short and long Fe…Fe distances along the direction of $\boldsymbol{c}$.

The displacive component of the modulation of atom *j* is described in the structural model by a three dimensional harmonic atomic displacement function $u_{jk}(\boldsymbol{q} \cdot \boldsymbol{r})$ so that :

$$x_{jk} = \bar{x}_{jk} + u_{jk}(\boldsymbol{q} \cdot \boldsymbol{r} + t),\ k=1,2,3 \qquad (18)$$

with $u_{jk}(\boldsymbol{q} \cdot \boldsymbol{r} + t) = \sum_{n=1}^{m} A^n sin(\boldsymbol{q} \cdot \boldsymbol{r} + t) + B^n cos(\boldsymbol{q} \cdot \boldsymbol{r} + t)$

where $\bar{x}_{jk}$ is the average position of atom *j* in the average structure, and *t* the initial phase.

The spin state ordering component is described by the spatial probability for a site at position $\boldsymbol{r}$ to be in the HS state, which in the harmonic approximation writes[70,79] :

$$\gamma_{HS}(\boldsymbol{r}) = \bar{\gamma}_{HS} + \eta \times cos(\boldsymbol{q} \cdot \boldsymbol{r} + t) \quad (19)$$

where $\bar{\gamma}_{HS}$ is the average HS fraction in the selected phase.

In such a case, the main and superstructure reflections do not contain the same structural information. The main reflections contain information on the average structure in the original ($\boldsymbol{a}$, $\boldsymbol{b}$, $\boldsymbol{c}$) unit cell, with an average disordered molecular structural conformation intermediate between LS and HS. The superstructure reflections are associated to the structure factor difference ΔF_{hkl} in the Argand diagram of figure 3(b), and as such characterize the structural reorganization and spin state long-range ordering in the direction of $\boldsymbol{c}$. The intensity of the superstructure reflections is proportional to the square of the order parameter of the symmetry breaking transition $I_{hkl} \propto \eta^2$, and can be used to follow the temperature dependence of the order parameter.

The second step of the thermal spin transition in [Fe(bapbpy)$_2$(NCS)$_2$] (from phase II to phase III) proceeds with a reduction of the unit cell volume almost divided by three with restauration of the lattice periodicity of phase I, together with a symmetry reduction from space group type *C2/c* to *C-1* (described in a non-conventional cell). The X-ray diffraction pattern of phase III exhibits a systematic splitting and enlargement of the Bragg peaks (figure 8c), resulting from the formation of different twin domains in the crystal; this process is described under details in section V.B.

C. Incommensurate HS/LS pattern development

The situation described above for the SCO compound [Fe(bapbpy)$_2$(NCS)$_2$] is common for multi-step spin transitions associated to a symmetry change in a multiple unit cell. The modulation wavevector is in these cases commensurate with the underlying crystal lattice. Alternative situations have been encountered for which the wavevector $\boldsymbol{q}$ is incommensurate, leading to aperiodic crystal structures, for which three dimensional periodicity is lost.[68,70–72] The corresponding X-ray diffraction pattern displays the presence of incommensurate satellite reflections at positions :

$$\boldsymbol{Q} + m\boldsymbol{q} = 2\pi(h\boldsymbol{a}^* + k\boldsymbol{b}^* + l\boldsymbol{c}^*) + m\boldsymbol{q} \quad (19)$$

The presence of isolated sharp satellite peaks (indexed with the modulation wavector $\boldsymbol{q}$) in the diffraction pattern is a direct signature of a new long-range ordering setting up. The incommensurate ordering may result from a modulation of the HS/LS distribution, a displacive modulation of the structure, or a conformational ordering of a fragment of the structure, or more frequently a combination of several of these modes.

The displacive and HS/LS ordering components are described by the functions $u_{jk}(\boldsymbol{q}\cdot\boldsymbol{r})$ and $\gamma_{HS}(\boldsymbol{r})$, as for the commensurate case, and the intensity of the satellite reflections represents a measure of the modulation amplitude, corresponding to the order parameter of the transition.

As a simple example, the SCO compound [Fe(abpt)$_2${N(CN)$_2$}$_2$] exhibits a structural architecture with two symmetry independent molecules (Fe1 and Fe2) stacked as alternating layers in the triclinic space group *P-1* (Fig. 9a). It undergoes a two-step thermal spin transition, associated to the successive spin state switching of the two iron sites. The structure presents at room temperature in the HS state an orientational disorder of the dicyanamide ligands (Fig. 9c). Thermal trapping of the HS state (room temperature) to the metastable HS state in a single crystal at 15 K has been achieved on an X-ray diffractometer. Upon this flash quenching, the diffraction pattern shows the appearance of sharp satellite reflections at positions $\boldsymbol{Q}+m\boldsymbol{q}$, with $\boldsymbol{q}=2\pi(0.338(5)\boldsymbol{a}^*+0.557(6)\boldsymbol{b}^*-0.047(5)\boldsymbol{c}^*)$ (Fig. 9d). The corresponding modulated structure has been refined in the superspace group *P-1(α,β,γ)* using harmonic displacive modulations for the two molecules (see Fe2 in Fig. 9e), and orientational modulation for the dicyanamide ligands (see N17 in Fig. 9e). Since the metastable state is completely HS, the spin state distribution is not modulated. The disorder to incommensurate order phase transition is thus described by two coupled distortion modes.

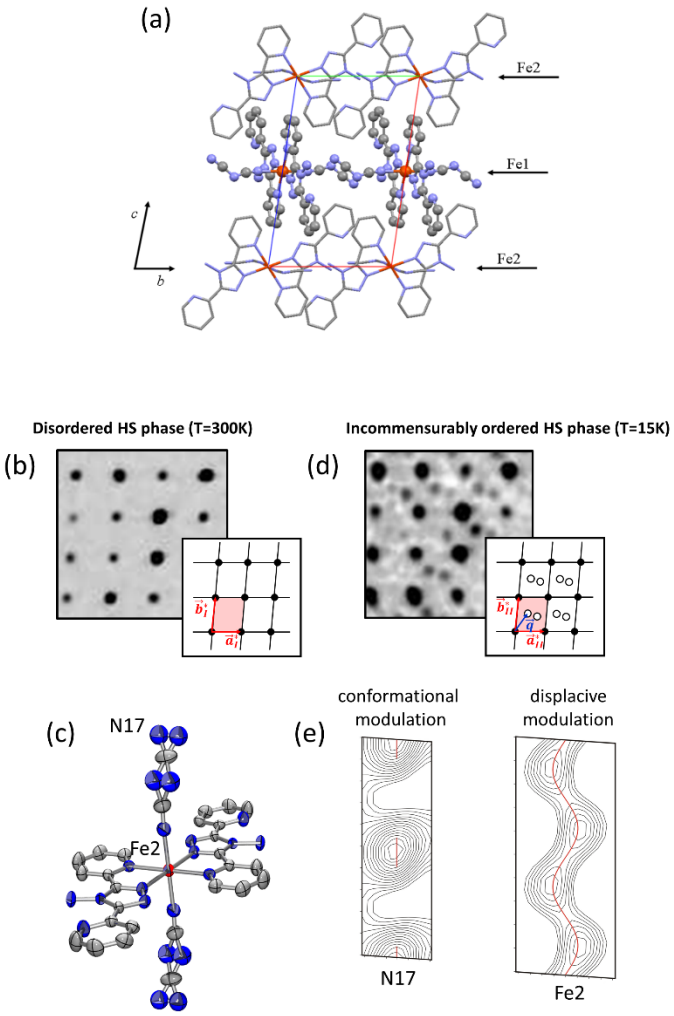

FIG. 9. (a) Crystal packing of $[Fe(abpt)_2\{N(CN)_2\}_2]$ displaying the stacking of Fe1 and Fe2 layers. (b) X-ray diffraction pattern in the disordered HS phase at 300K. (c) Disordered molecular structure at 300K. (c) X-ray diffraction pattern in the metastable quenched HS phase at 15K. (e) Fourier maps with displacive (Fe2) and orientation (N17) modulation functions. Adapted with permission from Sheu. *et al*. Inorg. Chem. **47**, 10866 (2008). Copyright 2008 American Chemical Society.

In insulator crystalline materials, such as SCO materials, transitions to incommensurate structures result from the competition between short-range interatomic or intermolecular forces of different ranges with similar magnitudes.[89] This process has been interpreted with models including competition between sublattices, or competition between first and second neighbor antagonist interactions, or frustration effects. For $[Fe(abpt)_2\{N(CN)_2\}_2]$, the incommensurability originates from frustration effects in intermolecular interactions involving the dicyanamide ligands, and misfit layer topology in the layer stacking of the crystal packing.

Incommensurability has been reported in only a few number of SCO materials, with sometimes a modulation of the spin state distribution, called spin-state concentration wave by the authors, in addition to a displacive component.[70–72] Such solid state mechanisms in SCO materials are remarkable from the structural point of view, and bring new functionalities and possibilities in the control of the SCO processes.

V. DOMAIN PATTERN IN SPIN CROSSOVER CRYSTALS

A. Classification of the structural phase transitions in spin-crossover crystals

Owing to the large molecular volume change associated to the spin state switching, combined with the elastic properties of the supporting crystalline medium, SCO materials exhibit usually severe local and/or collective structural distortions. For strongly cooperative SCO systems, a structural phase transition parallels the spin transition, which is therefore considered as strongly distortive. Depending on the crystallographic symmetry properties of the non-distorted and the distorted structural phases, a classification emerges as depicted in figure 10. The structural phase which has the maximum crystallographic symmetry of the considered SCO system is called the prototype phase. If no group-subgroup relationship exists between the respective phases across the transition, this latter is said reconstructive. Reconstructive phase transitions often take a path through an unstable and unobservable intermediate structure which is a common subgroup of the two phases. For distortive phase transitions, a small distortion leads to a new crystallographic phase which can be divided in two categories : isomorphous (or isostructural) for which there is no change of space group symmetry of the crystal, and non-isomorphous (or non-isostructural) at which a change of space group symmetry occurs. For example, the SCO compound $[Fe(btr)_2(NCS)_2].H_2O$, discussed below, presents an isomorphous thermal phase transition with space group *C2/c* in both the HS and LS phase (and also in the metastable light-induced HS phase), even though the transition is strongly cooperative with a 20 K thermal hysteresis.[90] The structural phase transitions in the two-step SCO $[Fe(bapbpy)_2(NCS)_2]$ discussed in the previous section are both non-isomorphous : from space group *C2/c* (phase I) to *C2/c* in a triple unit cell (phase II) to space group *C-1* (phase III). Non-isomorphous phase transitions can be further divided in ferroic and non-ferroic types, depending on whether a change of point group symmetry occurs (ferroic case). Finally, ferroic phase transitions for which the change of point group corresponds at the same time to a change of crystal class are called ferroelastic. Ferroelastic crystals may be considered as a type of ferroic crystal which are the mechanical analogues of ferroelectrics and ferromagnetics. Many phase transitions in SCO systems involve symmetry breaking processes, as recently reviewed[78], only a few of these are true ferroelastic transitions, and the resulting ferroelastic

domain pattern has rarely been studied in details. One of the most documented ferroelastic SCO compound is $[Fe(ptz)_6].(BF_4)_2$ which exhibits an abrupt phase transition from $\bar{3}$ (crystallographic space group $R\bar{3}$) to $\bar{1}$ (crystallographic space group $P\bar{1}$) point group symmetry reduction, thus generating 3 possible domain states, as described by Kusz and coworkers.[74]

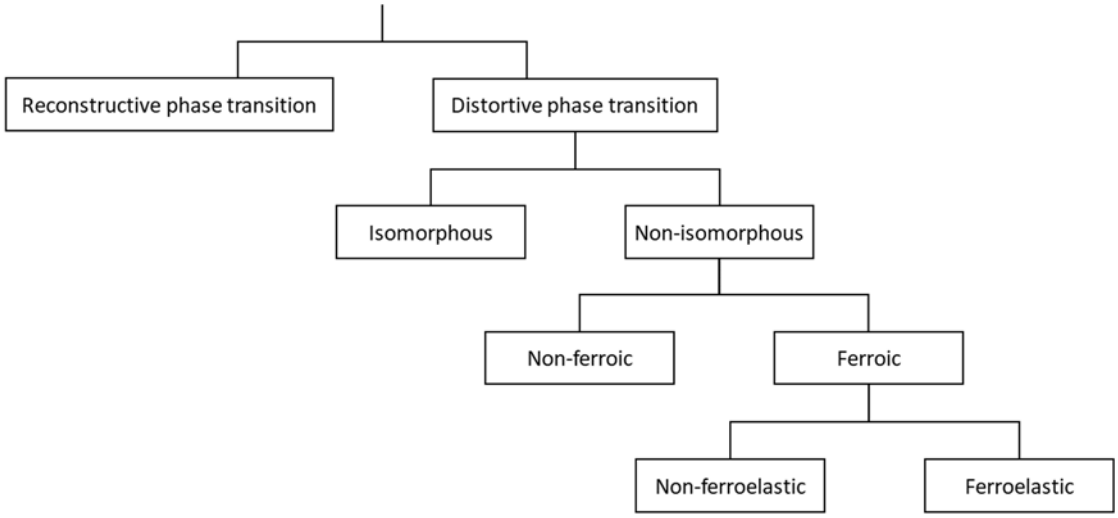

FIG. 10. Classification of structural phase transitions in SCO materials based on the symmetry reduction from the prototype phase to the daughter phase.

It is well recognized that the spin transition processes in the most cooperative SCO cases are associated to heterogeneous mechanisms with the formation and growth of spin state domains (called sometimes spin-domains, or spin-like domains).[91] Spin state domains are ascribed to a delimited spatial region of the crystal with a majority of HS or LS molecular spin state. Remarkable images of spin state domain nucleation, growth, and propagation of domain boundaries upon a HS/LS transition have been obtained using optical microscopy measurements down to a typical micrometer resolution.[15–19] The quantitative analysis of the propagation of the domain boundary allowed estimating the corresponding velocity, which is several orders of magnitude slower than the sound velocity in molecular crystals.[20] Micro-raman spectroscopy and atomic force microscopy have provided additional spin state mapping in single crystals.[92,93] The resulting interface separates two regions of the crystal with different spin state, this is a heterophase boundary, whose situation corresponds to case (a) in figure 11. Another situation (case(b) in figure 11) is associated to a ferroelastic structural transition, forming ferroelastic domains. The corresponding homophase interface separates regions with identical spin state. This major difference between the two concepts of domains will be illustrated in the next sections.

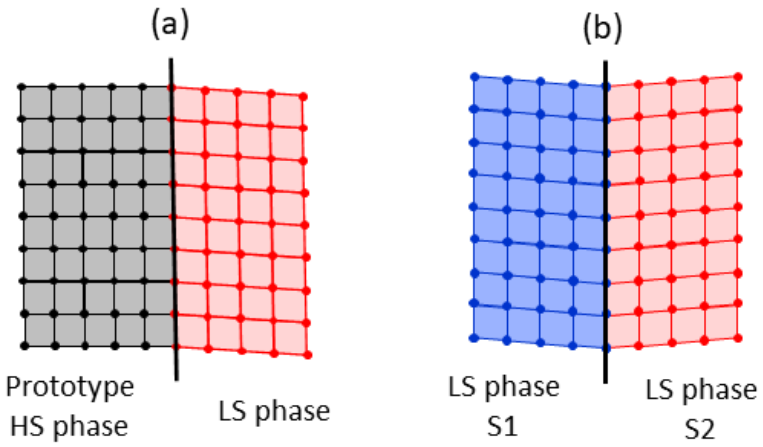

FIG. 11. (a) Schematic of the interface (depicted as a thick black line) separating two structural phases with different spin states (heterophase boundary). (b) Interface separating two ferroelastic domains (S1 and S2) with identical spin state (homophase boundary).

B. Ferroelastic domains in spin crossover

In SCO molecular crystals, most of the properties may well be understood by assessing the periodic crystal structure and its modification along the whole temperature range, and especially close to the spin transition temperature regime. The description of the ideal crystal structure is in some cases insufficient to capture the entire elements of the effective physical processes. A careful monitoring of microstructural features, such as grain size, grain boundaries, twins, dislocations may prove very fruitful. A subset of these microstructural effects is a direct consequence of the reduction of crystallographic symmetry, leading to the formation of a non-homogeneous, textured low-symmetry phase called a domain structure.[94] Among these, the formation of antiphase domains is due to a loss of translational symmetry, while the formation of ferroelastic domains is due to a loss of point-group symmetry.

The formation of such domains is very relevant for SCO molecular crystals considering the severe structural distortion associated to the spin state change, the elastic properties of the materials play therefore a central role in the transition mechanisms. Spin transitions have the potential to develop domain structure pattern in order to accommodate the strain in the crystal. This is an underestimated and still underlooked aspect which may impact strongly the spin transition mechanism and its dynamics. As a matter of fact, the observation of twins in a crystal structure determination is often considered as a nuisance but should be rather considered as an indication of structural instability which is important to be studied under details in the context of SCO materials.

The formation of a domain pattern during a symmetry reduction spin transition requires to consider several levels : (1) the crystal structure within the domain itself, (2) the orientation relationship between the different formed domains and the static pattern configuration, (3) the microscopic structure in the vicinity of the domain boundary.

For a bit of nomenclature, the high symmetry phase is called the prototype (or parent) phase, which undergoes a symmetry reduction phase transition into the daughter low-symmetry phase with lower point group symmetry. Resulting from this is a spatially non-homogeneous structure consisting of homogeneous regions (the domains) separated by contact regions called domain walls. All domains have the same microscopic structure defined by the same space group symmetry, but the structure in different domains has a different orientation. In the Landau theory, the formation of the domain structure follows from the existence of several equivalent solutions for the order parameter in the low-symmetry phase. As a consequence, through the point group symmetry reduction, several possible orientations of the domains, called domain states, are generated. Several domains may have the same orientation (and therefore domain states) but a different shape and position in the crystal. Following these concepts, Aizu proposed a definition of ferroelastic crystals : "Ferroelastic crystals have two or more equally stable orientation states, which can be switched from one state to another by the application of a suitable mechanical stress".[95] Such crystals may exhibit stress-strain hysteresis, and the domain structure can be visualized under a polarized-light microscope. The spontaneous symmetry breaking distortion of the prototype phase is described by the spontaneous strain tensor $\boldsymbol{\varepsilon}$, a symmetric traceless second rank tensor which possesses all the symmetry elements of the point group of the daughter phase.[94] In structural crystallography, a ferroelastic transition is also called a transformation twinning, and the domain states are called twin domains, or orientational domains.

As a first example, consider the transition from a prototype phase with point group symmetry 4/mmm ($a_T = b_T \neq c_T$) to a ferroic daughter phase with point group symmetry mmm ($a_O \neq b_O \neq c_O$). Under this symmetry reduction, the crystal unit cell distorts, and several ferroic domains of the daughter phase may nucleate. The corresponding unit cells and possible domain states are illustrated in figure 12 for a tetragonal I4/mmm to orthorhombic Fmmm space group symmetry reduction. The prototype high-symmetry unit cell is characterized by a regular tetragonal lattice, to which correspond a regular X-ray scattering pattern with well identified Bragg peaks (Fig. 12 bottom). In the given example, the diffraction pattern exhibits typical systematic absences for I centering cell. Upon the tetragonal to orthorhombic distortion, four domain states (noted O1, O2, O3, O4) are formed with equal probability. The crystal structure within each domain is identical, and their mutual orientation is related to each other by the various possible twin elements : $(110)_O$ and $(1\bar{1}0)_O$ twin planes with reference to the orthorhombic cell. The contact plane between two adjacent domains is oriented in a specific manner

in order to maintain a strain compatibility and certain lattice continuity. The possible domain boundaries are derived by symmetry arguments, as detailed hereafter in section V.D. In the present example, the contact planes between O1 and O2, and between O3 and O4 are clearly identified in figure 12. Note that each domain state can be transformed into another domain state by a uniaxial stress (e.g. O2 to O1 in figure 12).

The single crystal X-ray diffraction pattern, corresponding to this static domain structure, shows a direct signature of the domain formation; highlighted by Bragg peak splitting in four superimposed contributions related to the four domain orientations. Quantitatively, the angular mismatch between the different orthorhombic reciprocal lattices corresponds to the angular distortion of the crystal structure in direct space. The intensity ratio between the split peaks is directly proportional to the volume composition of the single crystal in the four domain states (usually called the twin fraction in structural crystallography).

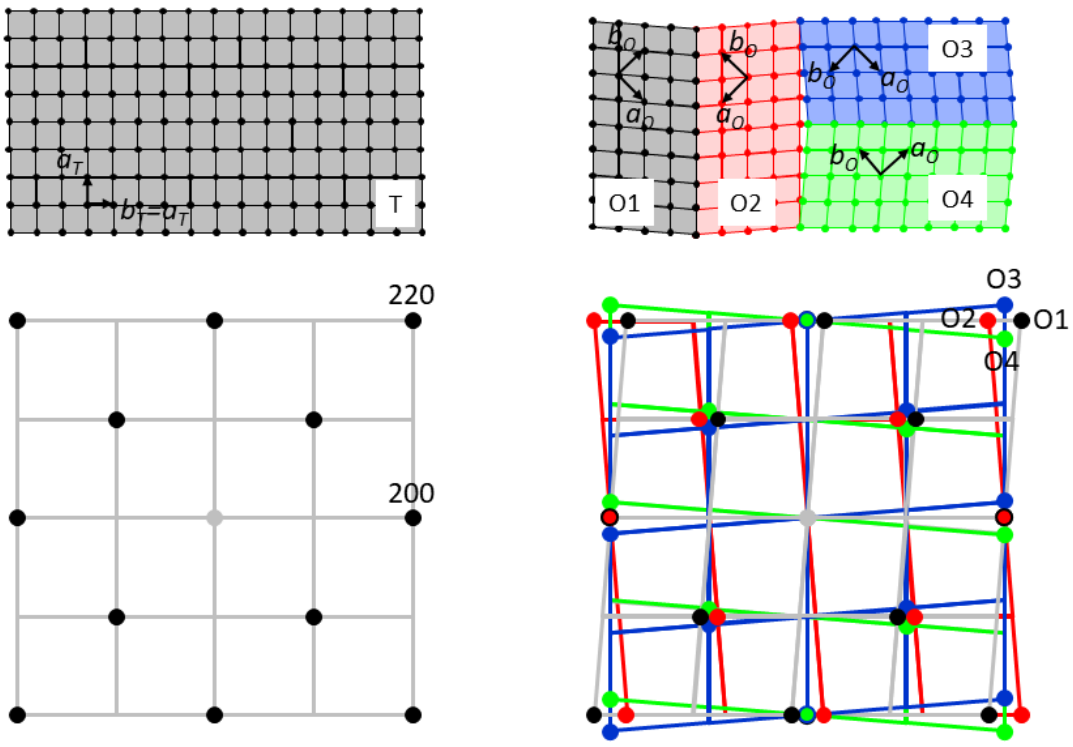

FIG. 12. (top) Schematic of the crystal lattices in the parent tetragonal phase (space group I4/mmm) and in the orthorhombic daughter phase (space group Fmmm) associated to the formation of four domain states (labelled O1, O2, O3, O4). Domain walls are identified between the different domains. (bottom) Schematic of the transformation of the single-crystal X-ray diffraction pattern during orthorhombic distortion and domain formation. Notice the diffraction peak splitting in the symmetry

breaking orthorhombic phase. Reproduced with permission from Tanatar *et al*. Phys. Rev. B **79**, 180508 (2009).[96] Copyright 2009 by the American Physical Society (APS).

Let us now consider a simple spin transition associated to a reduction of point group symmetry. For illustration purposes, we use the second step of the two-step spin transition of the $[Fe(bapbpy)_2(NCS)_2]$ compound discussed in previous sections. We have seen above that the intermediate phase (phase II) consists of an ordered [HS-LS-LS] pattern in a triple unit cell ($\boldsymbol{a}, \boldsymbol{b}, \boldsymbol{3c}$) with *C2/c* space group type. The transition from phase II to phase III is characterized by a unit cell reduction from ($\boldsymbol{a}, \boldsymbol{b}, \boldsymbol{3c}$) to ($\boldsymbol{a}, \boldsymbol{b}, \boldsymbol{c}$) and change of space group type *C2/c* to *C-1* (a non standard setting for triclinic space group). Correspondingly, the point group symmetry is reduced from 2/m to -1, with possibly the formation of domains of two domain states (noted S1 and S2).

The experimental reciprocal space mapping, derived from single crystal X-ray diffraction, in phase I and phase III is given in Figure 8. As can be seen, the regular monoclinic lattice of phase I undergoes a strong distortion to a triclinic lattice for phase III, together with a systematic Bragg peak splitting in two contributions. This is a direct signature of the formation of ferroelastic domains with the two possible domain states, whose orientations are related by a two-fold axis along the crystallographic $\boldsymbol{b}^*$ axis. This symmetry axis corresponds to the symmetry element lost during the structural phase transition. The static domain pattern in phase III has been characterized by Bedoui et al. in a polarized light optical microscopy experiment at 150 K, revealing a homogeneous domain pattern with micrometer sized domains of the two domain states (S1 and S2) with parallel domain walls perpendicular to the crystallographic direction of the $\boldsymbol{c}$ axis(FIG. 13).[92]

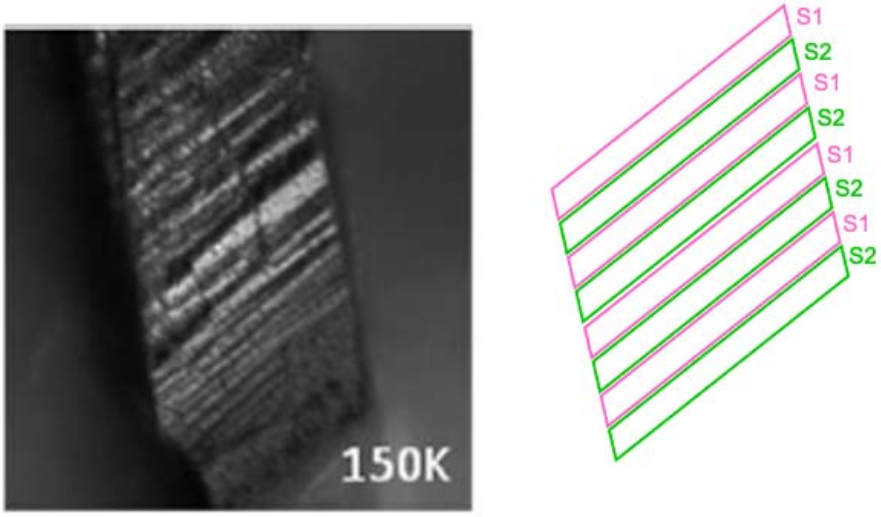

FIG. 13. (left) Polarized light optical microscopy of a single crystal of $[Fe(bapbpy)_2(NCS)_2]$ at 150 K in phase III. (right) Schematic of the static domain pattern with respect to the two domain states (S1 and S2). Adapted with permission from Bedoui *et al*. Chem. Phys. Lett. **499**, 94 (2010). Copyright 2010 Elsevier B.V. All rights reserved.

From a microscopic perspective, the transformation twinning occurring during the II->III structural phase transition results from a collective molecular displacement, connected to a triclinic deformation of the unit cell in order to accommodate the elastic strain generated by the molecular volume change along the [HS-LS-LS] to LS spin state switching. The formation of ferroelastic domains of mesoscopic size upon spin transitions is of major importance. For $[Fe(bapbpy)_2(NCS)_2]$, the kinetics of photo-induced transitions, and relaxation from the photoinduced state are strongly impacted by the formation of mesoscopic twins, as shown by the evolution of the unit cell volume and X-ray diffraction pattern along the I^{LIESST}->III relaxation at 40K after light-irradiation to the metastable I^{LIESST} phase (FIG. 14). It has been observed that the relaxation follows a three step process : the first unit cell volume contraction is associated to the I^{LIESST}->II spin transition, with formation of the self-ordered [HS-LS-LS] pattern. In a second step, the X-ray diffraction pattern shows modifications at constant unit cell volume, characterized by Bragg peak splitting originating from the formation of ferroelastic domains of the two domain states. Finally, in a late stage, the unit cell volume contracts to the final LS value.

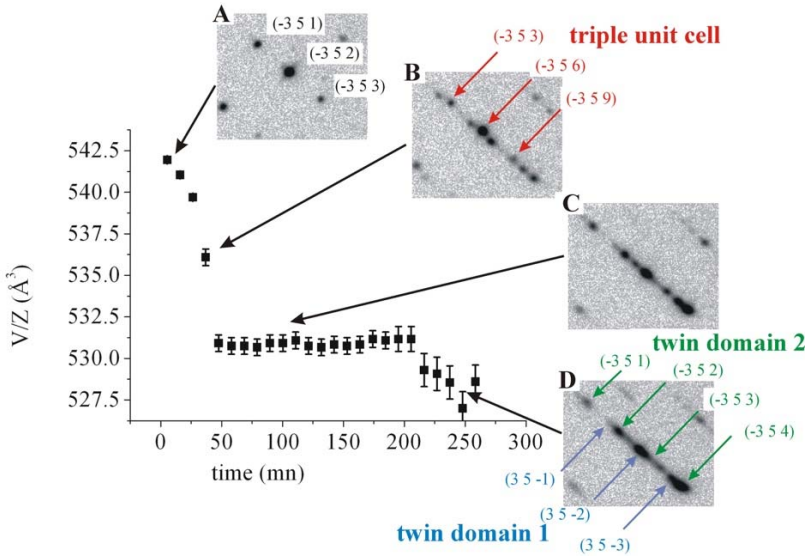

FIG. 14. Evolution of the unit cell volume per formula unit (V/Z) during the isothermal I^{LIESST}->III relaxation at 40 K from the photoinduced metastable state I^{LIESST}, and selected region of the diffraction pattern in $[Fe(bapbpy)_2(NCS)_2]$. Reproduced with permission from Pillet *et al*. Phys. Rev. B **86**, 064106 (2012). Copyright 2012 by the American Physical Society (APS).

This example illustrates the amount of information which can be gained from single crystal X-ray diffraction and reciprocal space mapping on the development of a mesostructured pattern in a SCO single crystal. It is important to stress that such information can absolutely not be obtained from X-ray diffraction on powder samples. A (hkl) reflection from two different domains in single crystal X-ray diffraction appears at two different and well separate positions in reciprocal space and can be distinguished. On the contrary, since obviously these reflections share the same d_{hkl} value, they contribute to the same diffraction cone in powder X-ray diffraction and cannot be individualized.

C. Spin state domain formation as seen from single crystal X-ray diffraction

Spin transition is conventionally characterized by the thermal transition curve, which can show very different behaviors, depending on the strength of the interactions between the SCO active sites. For weak interactions (weak cooperativity), the transition is gradual, the spatial distribution of the HS/LS molecules follows a Boltzmann statistics : the mechanism is called homogeneous. On the contrary, strongly interacting SCO active sites result in very cooperative processes, leading to abrupt transitions, sometimes associated to thermal hysteresis. In this latter case, cooperativity gives rise to a macroscopic free energy barrier for the phase transition in the solid state, which provides bistability to the system. The phase transformation occurs by nucleation and growth of domains of the thermodynamically stable phase. The spatial distribution of HS/LS SCO molecules is heterogeneous, showing a clustering of molecules with identical spin state in so called spin state domains (HS or LS domains), separated by boundary regions.

Key observations have been provided by optical microscopy under temperature variation on single crystal of strongly cooperative crystals, from which the spatiotemporal mapping of the spin-state change was recovered.[15–20] It has been observed that in general, nucleation of a reduced number of domains occurs in a rather deterministic and reproducible way. During the transition, several domains coexist and propagate with a well determined velocity. Owing to the large HS/LS molecular volume change, the formation of a domain generates large structural strain, especially in the vicinity of the domain boundary. Quite surprisingly, the orientation of the domain boundary appears also very well determined, with in most of the cases a flat surface and a specific orientation with respect to the crystal morphology (Fig. 15a), while in other cases, the domain boundary appears fuzzy (Fig. 15b).

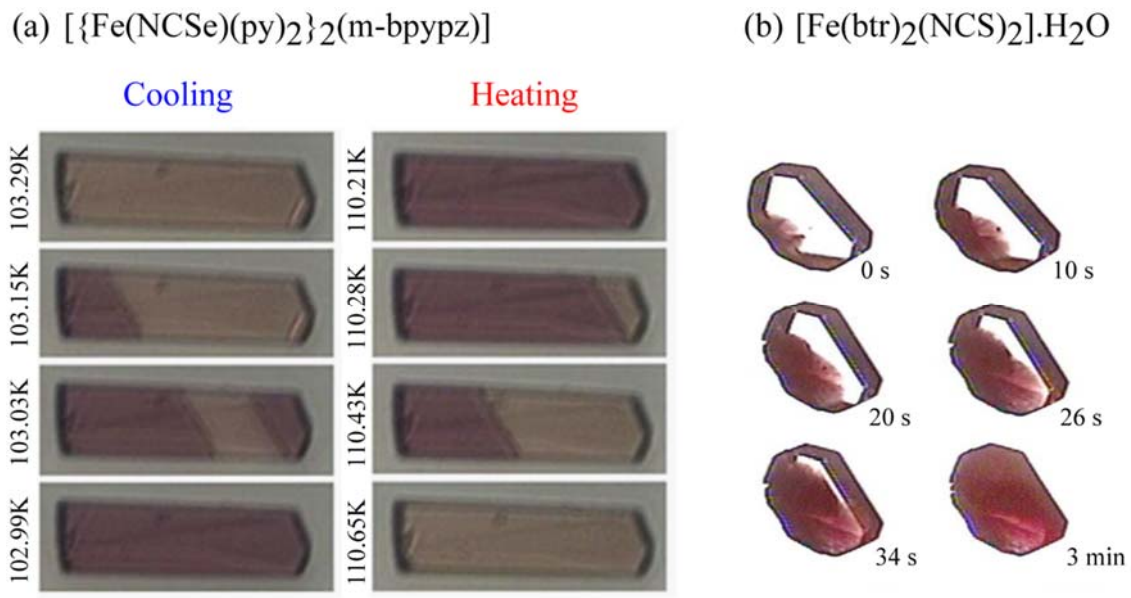

FIG. 15. Optical images of a single crystal of (a) the SCO material [{Fe(NCSe)(py)$_2$}$_2$(m-bpypz)] in the course of the thermal spin transition in the cooling and heating mode, and (b) the SCO material [Fe(btr)$_2$(NCS)$_2$].H$_2$O in isothermal condition at T = 105.5 K in the course of the HS to LS transition. Figure (a) reproduced from Varret *et al.* New J. Chem. 35, 2333 (2011) with permission from the Centre National de la Recherche Scientifique (CNRS) and The Royal Society of Chemistry (RSC). Figure (b) reproduced with permission under the creative commons license from Boukheddaden *et al.* Magnetochemistry 5, 21 (2019).

Single crystal X-ray diffraction, and reciprocal space mapping is a very powerful approach to capture the structural characteristics associated to domain nucleation and growth and decipher their dynamics.[90,97–103] We will use the SCO material [Fe(btr)$_2$(NCS)$_2$].H$_2$O (btr = 4,4'-bis-1,2,4-triazole) as a representative example. This compound exhibits a very abrupt spin transition at $T_{1/2}$=123K in the cooling branch and $T_{1/2}$=143K in the warming branch, with a 20K hysteresis. It crystallizes in the monoclinic space group *C2/c*, and the HS/LS structural transition is isostructural, without any space group change, and especially no symmetry breaking reduction which would lead to the formation of ferroelastic domains. The crystal structure of [Fe(btr)$_2$(NCS)$_2$].H$_2$O may be described as polymeric layers, built from Fe^{II} ions on a rectangular array connected by bidendate btr ligands. The layers are stacked along the ***c*** crystallographic axis through weak hydrogen bonds and van der Waals interactions. Accordingly, one can capture most of the structural features associated to the spin transition by considering only one regular polymeric layer. During the HS to LS transition, one can observe a single LS domain (in pink in figure 16) nucleating and growing in a single crystal. The evolution of the X-ray diffraction pattern exhibits a very specific behaviour as illustrated in figure 16. On the course of the HS to LS transformation, the X-ray Bragg peaks split systematically owing to the HS/LS structural

distortion. One peak corresponds to the fraction of the single crystal which is in the HS state, while the second peak, growing in intensity corresponds to the fraction of the crystal which is in the LS state, with a contracted unit cell. The peak displacement in reciprocal space corresponds to the difference in unit cell parameters between the two spin phases. As shown in figure 16, the profile of the HS and LS peak do not change significantly upon the spin transition, only the respective intensity follows the complete transformation of the HS lattice to the LS lattice. This means that the HS and LS domain size is much larger than the coherence length of the X-ray beam of the diffractometer. On a typical laboratory diffractometer, this coherence length is of the order of a few hundred nanometers in the transverse direction, and a few micrometers in the longitudinal direction. The built-up of diffuse scattered intensity in between the HS and LS diffraction peaks would correspond to the scattering of the strongly distorted domain walls. Such an effect is not detected in the present illustrative example.

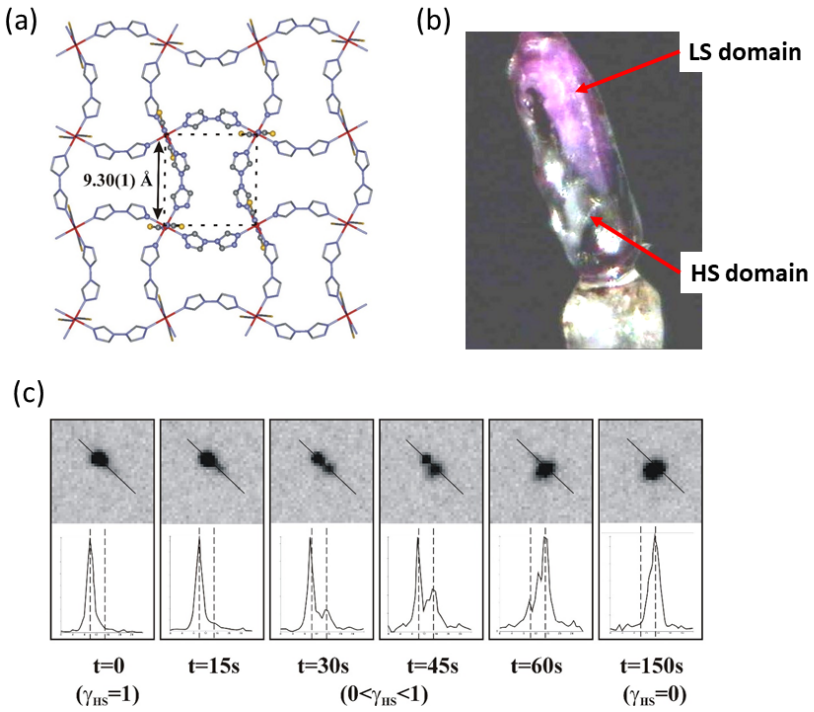

FIG. 16. (a) Layer structure of $[Fe(btr)_2(NCS)_2].H_2O$ in the HS state. (b) Microscope image of a single crystal during the HS to LS transition in the cooling mode. (c) Evolution of a selected region of the X-ray diffraction pattern as a function of time in isothermal condition at T = 117.2 K. Reproduced with permission from Pillet *et al*. Eur. Phys. J. B **38**, 541 (2004). With kind permission of The European Physical Journal (EPJ).

The intensity of the HS and LS peaks is directly proportional to the volume fraction of the HS and LS domains, so that the kinetics of the structural phase transformation can be derived by simply monitoring the evolution of the peak intensity. This has been done for $[Fe(btr)_2(NCS)_2].H_2O$, showing an indentical monotonous sigmoidal evolution for all Bragg peaks (fig. 17), with a short incubation time

during which the nucleation occurs, followed by a rapid acceleration of the transformation. This non-linear evolution has been adequately fitted to the Kolmogorov Johnson Mehl Avrami model (KJMA model) which has been historically introduced for describing phase transitions in metallurgy.[104,105] This model describes the evolution of the phase transformation as $c(t) = 1 - exp\{-[k(t-\tau_i)]^n\}$, where τ_i is the incubation time, k is the rate constant related to a characteristic transformation time $k = \frac{1}{\tau_{transf}}$, and n is the Avrami exponent which reflects the degree of heterogeneity and process dimensionality. In the context of SCO materials, this model is adequate to characterize the thermal spin transformation, and the light-induced transformation as well.[101]

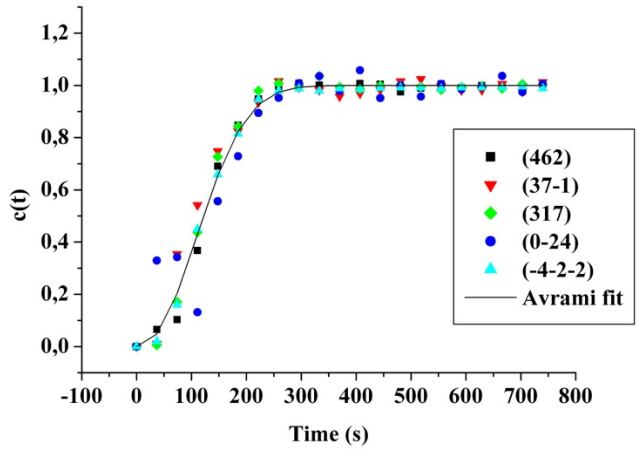

FIG. 17. Normalized integrated intensity $c(t) = \frac{I_{hkl}(t) - I_{hkl}(t\to 0)}{I_{hkl}(t\to\infty) - I_{hkl}(t\to 0)}$ for selected reflections during the thermal spin transition of $[Fe(btr)_2(NCS)_2].H_2O$. The experimental points have been fitted to the KJMA equation $c(t) = 1 - exp\{-[k(t-\tau_i)]^n\}$. Reproduced with permission from Pillet *et al*. Phys. Rev. B **74**, 140101 (2006). Copyright 2006 by the American Physical Society (APS).

Modelling of the spatiotemporal evolution of SCO systems has been achieved in the frame of various electro-elastic models, accounting for the interaction between SCO sites through either spring harmonic constants[106–108], or more elaborated anharmonic interactions of the Lennard Jones form.[109–111] These models reproduce the various homogeneous and heterogeneous transitions. One step further can be reached in the interpretation of the experimental X-ray diffraction mapping by calculating the Fourier transform of the configuration obtained from the simulation on the course of the spin transition. This has been reached by Nicolazzi et al. for a Monte Carlo simulation on a square 2D lattice, supposed to describe the structural layer of $[Fe(btr)_2(NCS)_2].H_2O$.[90] The results are illustrated in figure 18 for a strongly cooperative case. We can see that the HS structural configuration transforms to the LS configuration through the nucleation and growth of only two domains as a function of Monte

Carlo time (MCS). The corresponding calculated diffraction pattern presents a systematic Bragg peak splitting owing to the difference in HS/LS unit cell parameters. In addition, the two disoriented forming LS domains are associated to two LS peaks (LS1 and LS2) displaced in reciprocal space.

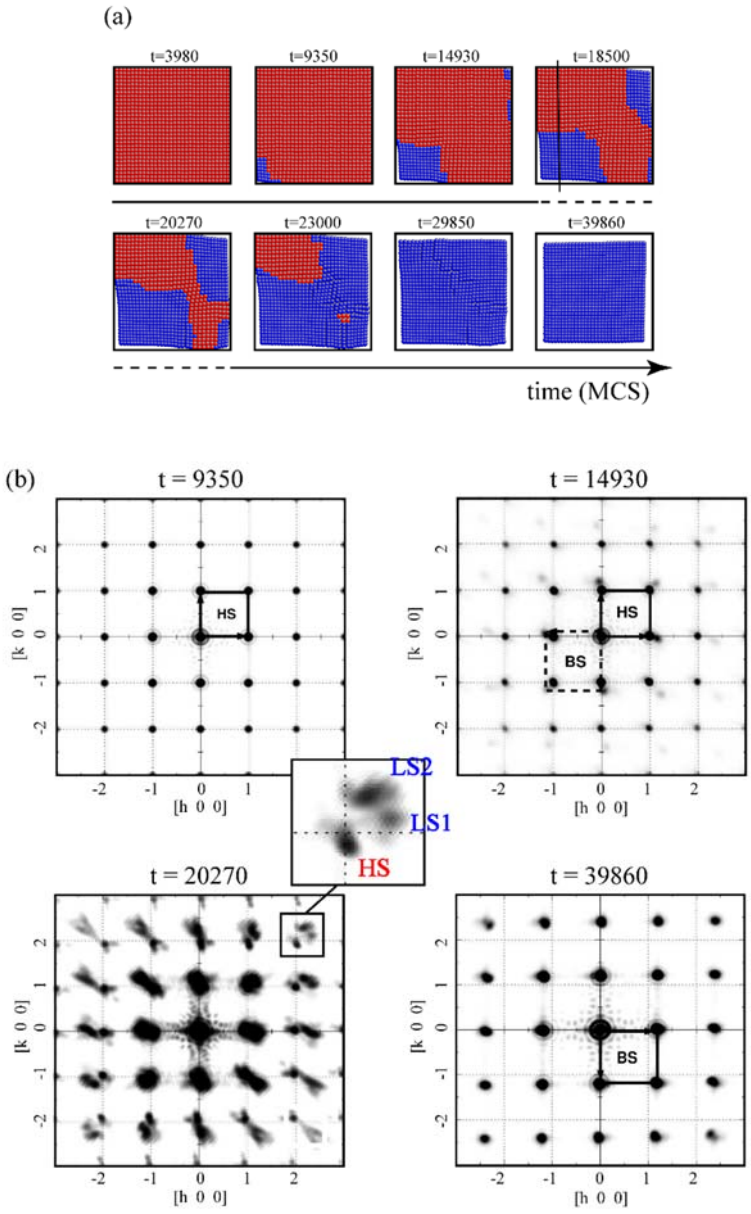

FIG. 18. (a) Simulated evolution of a square regular SCO system in a strongly cooperative case using the elastic anharmonic model (HS sites in red, LS sites in blue). (b) Calculated diffraction pattern for different Monte Carlo time, on the course of the HS to LS transformation. Diffraction peak splitting is characterized along the transition. Reproduced with permission from Nicolazzi *et al.* Phys. Rev. B **85**, 094101 (2012). Copyright 2012 by the American Physical Society (APS).[110–112]

For comparison, in the case of a weakly cooperative situation, the diffraction pattern shows a gradual diffraction peak displacement, owing to the gradual relaxation of the unit cell parameters. The empirical Vegard's law, which states that the unit cell parameters are proportional to the composition in a solid solution crystal, is fulfilled here.

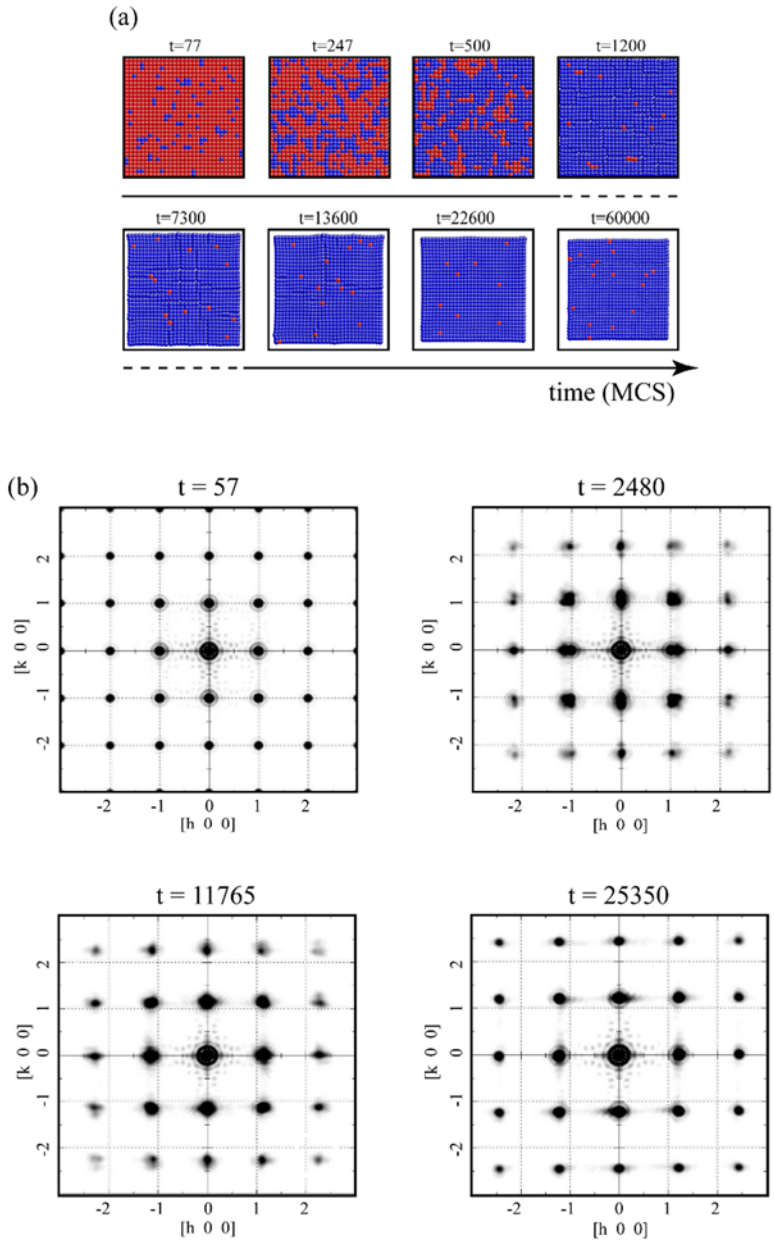

FIG. 19. (a) Simulated evolution of a square regular SCO system in a weakly cooperative case using the elastic anharmonic model (HS sites in red, LS sites in blue). (b) Calculated diffraction pattern for different Monte Carlo time, on the course of the HS to LS transformation. Diffraction peak displacement is characterized along the transition. Reproduced with permission from Nicolazzi *et al.* Phys. Rev. B **85**, 094101 (2012). Copyright 2012 by the American Physical Society (APS).[110–112]

Based on the two illustrative examples given above, it seems obvious that X-ray diffraction experiments conducted as a function of time and temperature (and/or optical excitation for the photo-induced transition regime) is perfectly adequate to extract very decisive qualitative and quantitative information on the spin transition process in the solid state both for the homogeneous case and the heterogeneous case.

D. Domain interfaces and symmetry of the domain pattern

The formation of a ferroelastic domain pattern below the phase transition temperature is a result of energy minimization owing to the created strain field. Elastic energy is reduced by the existence of domains, at the expense of domain wall energy, so that the sum of the two contributions becomes a minimum.

The orientation itself of the domain boundaries and the mechanical interaction between the two contacting phases determine to a large extent the configuration of the resulting pattern. In ferroelastics, the formation of the boundaries is governed by symmetry considerations, so that the phase boundary usually takes a prominent crystallographic orientation. The symmetry F of the ferroelastic phase is derived from the symmetry G of the prototype phase and defined by the $G \rightarrow F$ operating symmetry reduction. The symmetry elements relating the possible domain states are those symmetry elements which are lost during the ferroelastic transition. They map one domain state to another. For instance, symmetry mirror planes which are lost at a phase transition can become domain walls separating two continuous domains of the ferroelastic phase. Along this, Sapriel and Janovec defined a strainfree criterion for the permissible wall orientation so that the strain along all directions in the interface should be identical for the two separated domain states.[113,114] The procedure proposed by Sapriel results in pairs of permissible planar interfaces (mutually perpendicular to each other) in most of the cases. When no planar solution exists, the interfaces are stressed and deformed.

From a microscopic point of view, the continuity of the crystal lattice should be preserved to some extend across the interface, even though a slight disorientation of the domain states occurs in reality. This may be seen as a kind of epitaxy between the two connected phases. As a consequence, the interface is defined as a transition layer of effective width (a few unit cells thick) of the crystal where there is a continuous transition between the lattices of the two connected phases.

From a macroscopic point of view, the $G \rightarrow F$ symmetry reduction operating at a ferroelastic transition has some important repercussions on the measurable physical properties of the resulting multi-domain crystal. Macroscopic physical properties respect the point group symmetry of a mono-domain

crystal (Neumann's principle). Since the point group symmetry is decreased upon a ferroelastic transition, the symmetry of the properties of a single domain state are reduced accordingly. In addition, domain states are related to each other by the symmetry elements which are lost at the transition, so that the symmetry of the entire multi-domain crystal is higher than the symmetry F of the individual domain states. This rule is very important if one wants to design SCO materials with controlled symmetry properties, for which a prior control of the domain pattern has to be reached.

These symmetry arguments for ferroelastic domains may well be adapted to the case of spin state domains. It has been observed that in some situation, the macroscopic spin state domain interface exhibits a very well defined and reproducible orientation with respect to the crystal morphology, and therefore with respect to the crystallographic axis (Fig. 15a). This situation bears some similarities with the twin domain boundaries at which the interface separates two ferroelastic domains with the same crystal structure, but with a different spatial orientation, related by a true crystallographic symmetry element. The situation is different for the spin domains since the interface separates two domains with a different crystal structure, different unit cell parameters, possibly different crystallographic symmetries with or without any group sub-group relationship. Transposing the arguments, regularly oriented and planar interfaces separating spin state domains (case (a) in Fig. 15) should fulfill the strain compatibility requirement (Sapriel theory) and crystal lattice continuity. Strict strain compatibility can be relaxed to a minimum of strain difference, corresponding to a minimum of elastic energy buildup during the transition and stored at the interface. A similar argument has been developed by Boukheddaden et al. for explaining the interface orientation in the SCO compound $[\{Fe(NCSe)(py)_2\}_2(m\text{-bpypz})]$.[115] Correlatively, the orientation of the interface should correspond to the one minimizing atomic and molecular movement across the interface, in order to preserve the structural continuity.

VI. THE X-RAY DIFFRACTION PATTERN UNDER T PERTURBATION AND PHOTO-EXCITATION

X-ray diffraction measurements performed in fixed T, P conditions provide a detailed structural characterization of the studied material as a single picture. Experiments carried out as a function of an external control parameter offer the additional opportunity to monitor the structural response under the perturbation, a kind of "structural susceptibility". In this direction it is very informative to define and explore the complete structural phase diagram on the hypersurface of the external parameters (e.g. (P,T) phase diagram, (T,hv) phase diagram). In a further perspective, external parameters provide an efficient way to drive the system in certain regions of the phase diagram, which are interesting in terms of properties. For instance, driving a SCO single crystal in a polar structural phase may possibly

couple ferroelectricity with the spin transition itself. By varying P or T, the system explores the hypersurface of the ground state, while using light-irradiation drives the system on the hypersurface of the excited states from which it will further evolves.

A. Crystal lattice deformation upon a variation of temperature

Structural determination as a function of temperature by single crystal or powder X-ray diffraction is experimentally quite conventional. As exemplified by a careful study on the gradual SCO compound $[Fe(PM\text{-}Aza)_2(NCS)_2]$[116] or the strongly cooperative SCO compounds $[Fe(btr)_2(NCS)_2].H_2O$,[90] and the different members of the $[Fe(Rtz)_6].(BF_4)_2$ family (Rtz = ptz, mtz, etz, ptz)[117–120], a multitemperature analysis allows deconvoluting precisely the structural distortion associated to the spin state switching itself from the response of the crystal lattice to the temperature variation.

In general, the temperature dependence of the unit cell parameters mirrors nicely the transition curve $\gamma_{HS}(T)$ derived from thermomagnetic measurements. For a gradual transition, this results from the adequation of the mean field approximation. For a cooperative transition, the abrupt character, the hysteresis, and the phase separation are also perfectly matched.

The temperature dependence of the unit cell parameters $x(T)$ can be formalized accounting for the lattice deformation upon the spin transition and the thermal expansion of the HS and LS lattices through[120,121] :

$$x(T) = [\mathbf{1} + \boldsymbol{\alpha}(T - T_0) + \boldsymbol{\varepsilon}\gamma_{HS}(T)]x_{LS}(T_0) \quad (21)$$

Where $\boldsymbol{\varepsilon}$ and $\boldsymbol{\alpha}$ are the temperature independent deformation tensor and thermal expansion tensor respectively. The deformation tensor $\boldsymbol{\varepsilon}$ does not represent a pure shear strain, but accounts also for the HS to LS unit cell volume change through :

$$\Delta V_{HS-LS} = V_{LS} Tr(\boldsymbol{\varepsilon}) \quad (22)$$

The tensor $\boldsymbol{\varepsilon}$ is therefore different from the spontaneous strain tensor introduced above for ferroelastic transitions.

B. Mechanism of the LS to HS light induced and HS to LS relaxation processes from kinetic powder X-ray diffraction

Structural analysis on the course of a photo-induced spin transition and subsequent HS to LS relaxation is very important for studying the associated mechanisms on a dynamic scale. Investigations of the

evolution of the structures under permanent irradiation at relevant and controlled temperatures (usually cryogenic temperatures for the LIESST, reverse-LIESST and relaxation phenomena) has for instance revealed new metastable hidden phases[122–124], multi-step processes or multimetastability[10,75] (e.g. thermally quenched structure different from the photoinduced phase).

Different dynamics have been predicted from Ising-like and mechanoelastic models of SCO, indicating the importance of nucleation and domain growth, short-range fluctuations, elastic strain, depending on various intrinsic parameters (elastic properties of the solid, strength of the interactions).[109–111,125]

Detailed information can be obtained through kinetic X-ray crystallography, by monitoring the evolution of the single crystal or powder diffraction pattern (diffraction peak position, intensity, width) as a function of time using external conditions as control parameters (temperature, irradiation wavelength, light intensity). In a very simple case, a continuous displacement of Bragg peaks is observed, corresponding to a progressive evolution of the unit cell volume as a function of the HS-LS molecular switching. The instantaneous distribution of HS/LS molecules is random in the solid, and the Vegard's law can be used to estimate the HS fraction. The spin transition process is homogeneous. In a more cooperative case, a splitting of the Bragg peaks is observed, attributed to phase separation. This situation has been characterized for the SCO compound $[Fe_xZn_{1-x}(phen)_2(NCS)_2]$ as a function of zinc metal dilution through kinetic powder X-ray diffraction (Fig. 20).[126] Fitting the different components in the diffraction pattern as a function of photo-excitation time or relaxation time allows deducing kinetic curves of the advancement of the phase transition. This method has been used to fit the HS to LS relaxation curves after photoexcitation as a function of temperature using the KJMA kinetic model, which describes the volume fraction of the LS transformed phase as $c(t) = 1 - exp\{-[k(t-\tau_i)]^n\}$. For $[Fe_xZn_{1-x}(phen)_2(NCS)_2]$, the relaxation rate constants k have been derived at variable temperature for the different dilution ratios. As can be seen on Fig. 21, the KJMA model correctly fits the experimental measurements. The derived rate constants follow an Arrhenius behavior (linear dependence of $ln(k)$ with reciprocal temperature $1/T$), signature of a thermally activated relaxation process, whose activation energy to LS domain nucleation and growth depends on the dilution ratio ($E_a(x=1) = 478\ cm^{-1}$, $E_a(x=0.5) = 519\ cm^{-1}$).

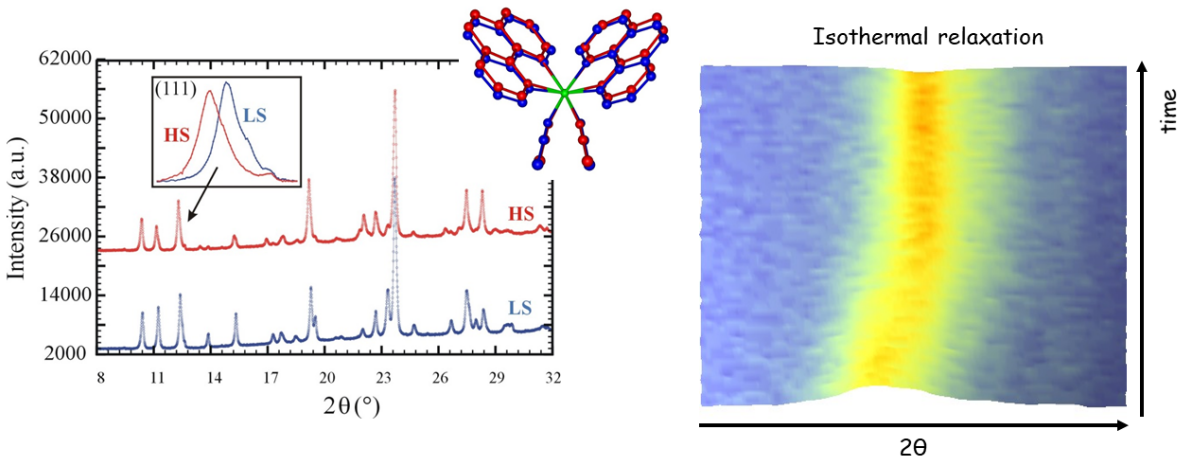

FIG. 20. (left) Diffraction pattern of the SCO compound $[Fe(phen)_2(NCS)_2]$ at 13 K in the LS (in blue) state and HS (in red) state. Inset : 2θ displacement of the (111) diffraction peak upon HS to LS relaxation. (right) Evolution of the (111) peak as a function of time during the HS to LS relaxation. Reproduced with permission from Lebedev *et al*. IOP Conf. Ser.: Mater. Sci. Eng. **5**, 012025 (2009). © IOP Publishing. Reproduced with permission. All rights reserved.

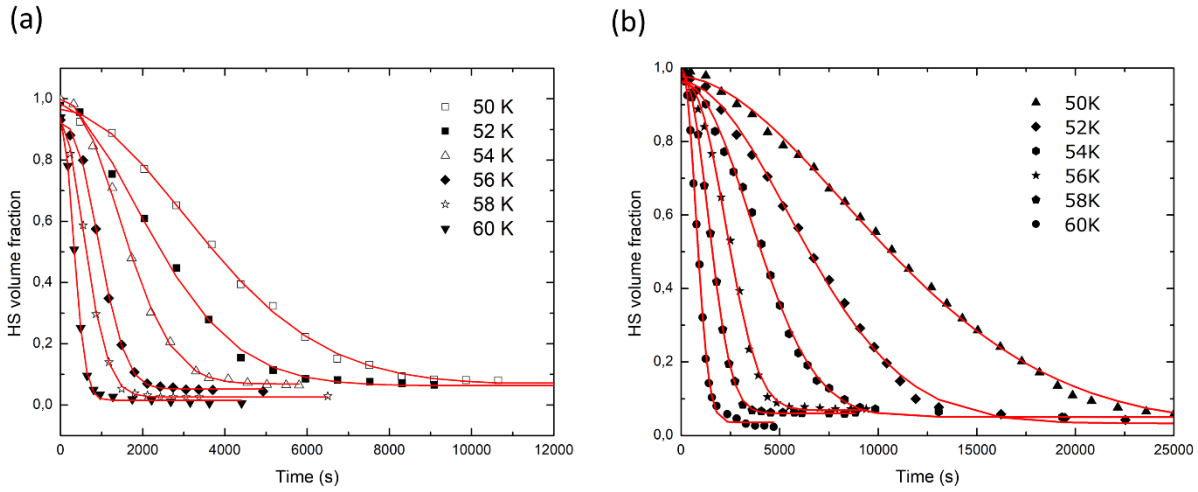

FIG. 21. Relaxation kinetics for (a) $[Fe(phen)_2(NCS)_2]$ and (b) $[Fe_{0.5}Zn_{0.5}(phen)_2(NCS)_2]$ as a function of temperature. Solid lines are least squares fit to the KJMA model. Reproduced with permission from Lebedev *et al*. IOP Conf. Ser.: Mater. Sci. Eng. **5**, 012025 (2009). © IOP Publishing. Reproduced with permission. All rights reserved.

More intricate dynamics can also be evidenced. The SCO compound $[Fe(pz)Pt(CN)_4]\cdot 2.6H_2O$ (pz = pyrazine) shows an abrupt spin transition with a wide thermal hysteresis loop near room temperature.

Its crystal structure may be pictured as a 3D pillared-layer type porous framework built from cyano-bridged Fe^{II}-Pt^{II} bimetallic layers bridged by pyrazine groups. Delagado et al. used synchrotron kinetic powder X-ray diffraction to probe the structural distortion and reorganization accompanying the light-induced and relaxation spin transitions at cryogenic temperature.[127] The relaxation process after light excitation shows a complex kinetics. Initially, the light-induced diffraction pattern corresponds to a pure HS phase. The diffraction peaks then shift to higher diffraction angle and broaden, indicating the progressive decrease in unit cell volume upon the HS-to-LS relaxation and development of structural inhomogeneities respectively. Each Bragg peaks separates in three contributions : the pure initial HS phase, the pure final LS phase, and an intermediate mixed HS/LS phase. The intensity evolution of the three contributions has been analyzed quantitatively to propose a kinetic model of the solid state process with a distribution of relaxation-rate constants.

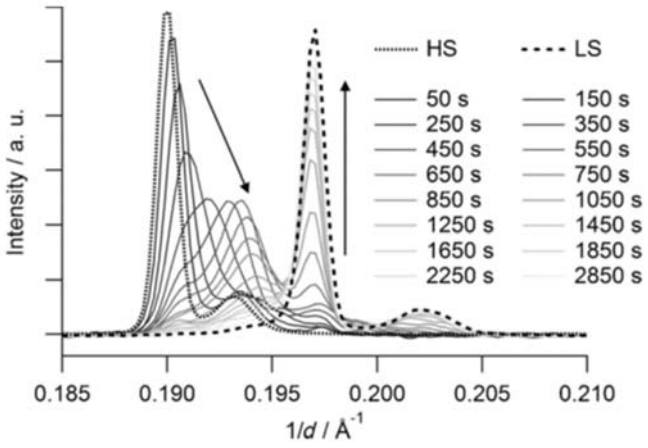

FIG. 22. Evolution of a selected region of the diffraction pattern of $[Fe(pz)Pt(CN)_4]\cdot 2.6H_2O$ at 10K as a function of time along the HS to LS relaxation. Reproduced with permission from Delgado *et al*. Chem. Eur. J. **21**, 3664 (2015). Copyright 2015 by John Wiley and Sons.

VII. SUMMARY AND OUTLOOK

Deriving predictable structure-properties relationship in SCO is fundamental in order to reach a structure-based design of materials with appropriate and enhanced properties. Conventional structural X-ray crystallography has been a mature field in providing precise structural descriptions of all the SCO materials elaborated to date. Specific mechanisms have been elucidated, such as the origin of multistep transitions, symmetry breaking transitions, origin of different behaviors for different SCO polymorphs, structural response to external stimuli, by tracking the crystal structure as a function of temperature, pressure, or light irradiation.

It is however quite often necessary to explore the structure beyond the spatially and time averaged picture. Examples have been discussed in the present tutorial for which advanced X-ray crystallography methods have been pushed towards a multiscale description of the structural processes, by focusing directly on the measured data in reciprocal space. A 3D mapping of the scattered intensity in reciprocal space allows identifying (i) the presence or apparition of sublattice reflections originating from a symmetry breaking transition and commensurate or incommensurate modulation of the crystal structure, (ii) diffuse scattering related to short-range correlations in the spin state distribution for instance, (iii) Bragg peak splitting due to ferroelastic transitions or spin-state domain patterns. Kinetic single-crystal or powder X-ray crystallography offers the opportunity to associate the measured diffraction intensity to phase transition dynamic models (first-order kinetics, Avrami kinetics).

There are a number of new challenging issues in which X-ray crystallography could bring decisive information in order to further understand precisely the operating spin transition mechanisms. In the field of SCO nanoparticles and nanocomposites, the structural organization and structural behavior is difficult to be studied properly through powder X-ray diffraction techniques. The pair distribution function approach could be at the forefront of such exploratory investigations, experimental instruments have been designed to perform rapid and systematic total scattering measurements in various sample environment conditions (T variation, controlled gas or humidity atmosphere). The formation of spin state domain and ferroelastic domain pattern, intimately connected to the spin state switching, is fundamental in the understanding of strongly cooperative SCO processes. The mechanical behavior of a ferroelastic crystal is influenced in a crucial way by its domain pattern. It is a great challenge to be able to control the nucleation and the mobility of the domain walls in SCO compounds, on which depends many of their potential applications. X-ray crystallography and structural mapping in single crystals should play a key role in understanding these processes.

ACKNOWLEDGMENTS

The author is indebted to El-Eulmi Bendeif, Dominik Schaniel (Laboratoire CRM2, Nancy, France) and Philippe Guionneau (ICMCB, Bordeaux, France) for many stimulating discussions. This work is supported by the Université de Lorraine, and the Centre National de la Recherche Scientifique (CNRS).

DATA AVAILABILITY

The data that support the findings of this study are available from the corresponding author upon reasonable request.

REFERENCES

[1] P. Gütlich and H.A. Goodwin, editors , *Spin Crossover in Transition Metal Compounds* (Springer, Berlin ; New York, 2004).
[2] M.A. Halcrow, editor , *Spin-Crossover Materials: Properties and Applications* (Wiley, Chichester, West Sussex, United Kingdom, 2013).
[3] P. Gütlich, A. Hauser, and H. Spiering, Angew. Chem. Int. Ed. **33**, 2024 (1994).
[4] M.A. Halcrow, Chem. Soc. Rev. **40**, 4119 (2011).
[5] S. Brooker, Chem. Soc. Rev. **44**, 2880 (2015).
[6] M.A. Halcrow, Chem. Lett. **43**, 1178 (2014).
[7] M.A. Halcrow, I. Capel Berdiell, C.M. Pask, and R. Kulmaczewski, Inorg. Chem. **58**, 9811 (2019).
[8] G.S. Matouzenko, A. Bousseksou, S. Lecocq, P.J. van Koningsbruggen, M. Perrin, O. Kahn, and A. Collet, Inorg. Chem. **36**, 5869 (1997).
[9] J. Tao, R.-J. Wei, R.-B. Huang, and L.-S. Zheng, Chem. Soc. Rev. **41**, 703 (2012).
[10] G.A. Craig, J.S. Costa, S.J. Teat, O. Roubeau, D.S. Yufit, J.A.K. Howard, and G. Aromí, Inorg. Chem. **52**, 7203 (2013).
[11] D. Chernyshov, M. Hostettler, K.W. Törnroos, and H.-B. Bürgi, Angew. Chem. Int. Ed. **42**, 3825 (2003).
[12] P. Guionneau, F. Le Gac, A. Kaiba, J.S. Costa, D. Chasseau, and J.-F. Létard, Chem. Commun. 3723 (2007).
[13] H. Spiering, in *Spin Crossover in Transition Metal Compounds III* (Springer-Verlag, Berlin/Heidelberg, 2004), pp. 171–195.
[14] H. Spiering and N. Willenbacher, J. Phys.: Condens. Matter **1**, 10089 (1989).
[15] F. Varret, A. Slimani, K. Boukheddaden, C. Chong, H. Mishra, E. Collet, J. Haasnoot, and S. Pillet, New J. Chem. **35**, 2333 (2011).
[16] M. Sy, R. Traiche, H. Fourati, Y. Singh, F. Varret, and K. Boukheddaden, J. Phys. Chem. C **122**, 20952 (2018).
[17] A. Slimani, F. Varret, K. Boukheddaden, C. Chong, H. Mishra, J. Haasnoot, and S. Pillet, Phys. Rev. B **84**, 094442 (2011).
[18] M. Sy, D. Garrot, A. Slimani, M. Paez-Espejo, F. Varret, and K. Boukheddaden, Angew. Chem. Int. Ed. **55**, 1755 (2016).
[19] H. Fourati, G. Bouchez, M. Paez-Espejo, S. Triki, and K. Boukheddaden, Crystals **9**, 46 (2019).
[20] A. Slimani, F. Varret, K. Boukheddaden, D. Garrot, H. Oubouchou, and S. Kaizaki, Phys. Rev. Lett. **110**, 087208 (2013).
[21] K. Boukheddaden, H. Fourati, Y. Singh, and G. Chastanet, Magnetochemistry **5**, 21 (2019).
[22] P. Guionneau, M. Marchivie, G. Bravic, J.-F. Létard, and D. Chasseau, in *Spin Crossover in Transition Metal Compounds II* (Springer Berlin Heidelberg, Berlin, Heidelberg, 2004), pp. 97–128.
[23] P. Guionneau, Dalton Trans. **43**, 382 (2014).
[24] P. Guionneau and E. Collet, in *Spin-Crossover Materials*, edited by M.A. Halcrow (John Wiley & Sons Ltd, Oxford, UK, 2013), pp. 507–526.
[25] E. Collet and P. Guionneau, C. R. Chim. **21**, 1133 (2018).
[26] K. Ridier, G.A. Craig, F. Damay, T. Fennell, M. Murrie, and G. Chaboussant, Phys. Rev. B **95**, 094403 (2017).
[27] M. Mikolasek, K. Ridier, D. Bessas, V. Cerantola, G. Félix, G. Chaboussant, M. Piedrahita-Bello, E. Angulo-Cervera, L. Godard, W. Nicolazzi, L. Salmon, G. Molnár, and A. Bousseksou, J. Phys. Chem. Lett. **10**, 1511 (2019).
[28] Y. Jiang, L.C. Liu, H.M. Müller-Werkmeister, C. Lu, D. Zhang, R.L. Field, A. Sarracini, G. Moriena, E. Collet, and R.J.D. Miller, Angew. Chem. Int. Ed. **56**, 7130 (2017).
[29] R.M. van der Veen, O.-H. Kwon, A. Tissot, A. Hauser, and A.H. Zewail, Nature Chem. **5**, 395 (2013).

[30] T. Egami and S.J.L. Billinge, *Underneath the Bragg Peaks: Structural Analysis of Complex Materials* (Pergamon, Kiddington, Oxford, UK ; Boston, 2003).
[31] P. Coppens, D.V. Fomitchev, M.D. Carducci, and K. Culp, J. Chem. Soc., Dalton Trans. 865 (1998).
[32] W.K. Fullagar, G. Wu, C. Kim, L. Ribaud, G. Sagerman, and P. Coppens, J Synchrotron Rad **7**, 229 (2000).
[33] V. Legrand, S. Pillet, H.-P. Weber, M. Souhassou, J.-F. Létard, P. Guionneau, and C. Lecomte, J. Appl. Crystallogr. **40**, 1076 (2007).
[34] Y. Ozawa, M.R. Pressprich, and P. Coppens, J. Appl. Crystallogr. **31**, 128 (1998).
[35] L.E. Hatcher, J.M. Skelton, M.R. Warren, and P.R. Raithby, Acc. Chem. Res. **52**, 1079 (2019).
[36] L.E. Hatcher, M.R. Warren, A.R. Pallipurath, L.K. Saunders, and J.M. Skelton, in *21st Century Challenges in Chemical Crystallography I*, edited by D.M.P. Mingos and P.R. Raithby (Springer International Publishing, Cham, 2020), pp. 199–238.
[37] P. Coppens and B. Fournier, J. Synchrotron Rad. **22**, 280 (2015).
[38] F. Volatron, L. Catala, E. Rivière, A. Gloter, O. Stéphan, and T. Mallah, Inorg. Chem. **47**, 6584 (2008).
[39] E. Coronado, J.R. Galán-Mascarós, M. Monrabal-Capilla, J. García-Martínez, and P. Pardo-Ibáñez, Adv. Mater. **19**, 1359 (2007).
[40] L. Salmon and L. Catala, C. R. Chim. **21**, 1230 (2018).
[41] P. Durand, S. Pillet, E.-E. Bendeif, C. Carteret, M. Bouazaoui, H. El Hamzaoui, B. Capoen, L. Salmon, S. Hébert, J. Ghanbaja, L. Aranda, and D. Schaniel, J. Mater. Chem. C **1**, 1933 (2013).
[42] A. Grosjean, P. Négrier, P. Bordet, C. Etrillard, D. Mondieig, S. Pechev, E. Lebraud, J.-F. Létard, and P. Guionneau, Eur. J. Inorg. Chem. **2013**, 796 (2013).
[43] A. Michalowicz, J. Moscovici, J. Charton, F. Sandid, F. Benamrane, and Y. Garcia, J. Synchrotron Rad. **8**, 701 (2001).
[44] A. Michalowicz, J. Moscovici, B. Ducourant, D. Cracco, and O. Kahn, Chem. Mater. **7**, 1833 (n.d.).
[45] H. Spiering, T. Kohlhaas, H. Romstedt, A. Hauser, C. Bruns-Yilmaz, J. Kusz, and P. Gütlich, Coord. Chem. Rev. **190–192**, 629 (1999).
[46] I.I. Vorontsov and P. Coppens, J. Synchrotron Rad. **12**, 488 (2005).
[47] D. Chernyshov, N. Klinduhov, K.W. Törnroos, M. Hostettler, B. Vangdal, and H.-B. Bürgi, Phys. Rev. B **76**, 014406 (2007).
[48] G.S. Matouzenko, A. Bousseksou, S.A. Borshch, M. Perrin, S. Zein, L. Salmon, G. Molnar, and S. Lecocq, Inorg. Chem. **43**, 227 (2004).
[49] G.S. Matouzenko, D. Luneau, G. Molnár, N. Ould-Moussa, S. Zein, S.A. Borshch, A. Bousseksou, and F. Averseng, Eur. J. Inorg. Chem. **2006**, 2671 (2006).
[50] D. Chernyshov, B. Vangdal, K.W. Törnroos, and H.-B. Bürgi, New J. Chem. **33**, 1277 (2009).
[51] T. Delgado, A. Tissot, L. Guénée, A. Hauser, F.J. Valverde-Muñoz, M. Seredyuk, J.A. Real, S. Pillet, E.-E. Bendeif, and C. Besnard, J. Am. Chem. Soc. **140**, 12870 (2018).
[52] A. Naim, Y. Bouhadja, M. Cortijo, E. Duverger-Nédellec, H.D. Flack, E. Freysz, P. Guionneau, A. Iazzolino, A. Ould Hamouda, P. Rosa, O. Stefańczyk, Á. Valentín-Pérez, and M. Zeggar, Inorg. Chem. **57**, 14501 (2018).
[53] A.O. Hamouda, F. Dutin, J. Degert, M. Tondusson, A. Naim, P. Rosa, and E. Freysz, J. Phys. Chem. Lett. **10**, 5975 (2019).
[54] R.T. Acha and M. Pilkington, CrystEngComm **17**, 8897 (2015).
[55] C. Bartual-Murgui, L. Piñeiro-López, F.J. Valverde-Muñoz, M.C. Muñoz, M. Seredyuk, and J.A. Real, Inorg. Chem. **56**, 13535 (2017).
[56] I.A. Gural'skiy, O.I. Kucheriv, S.I. Shylin, V. Ksenofontov, R.A. Polunin, and I.O. Fritsky, Chem. Eur. J. **21**, 18076 (2015).
[57] V.B. Jakobsen, L. O'Brien, G. Novitchi, H. Müller-Bunz, A.-L. Barra, and G.G. Morgan, Eur. J. Inorg. Chem. **41**, 4405 (2019).
[58] W. Liu, X. Bao, L.-L. Mao, J. Tucek, R. Zboril, J.-L. Liu, F.-S. Guo, Z.-P. Ni, and M.-L. Tong, Chem. Commun. **50**, 4059 (2014).
[59] T. Romero-Morcillo, F.J. Valverde-Muniz, M. Carmen Munoz, J.M. Herrera, E. Colacio, and J.A. Real, RSC Adv. **5**, 69782 (2015).

[60] H.D. Flack, Acta Cryst. **A39**, 876 (1983).
[61] S. Parsons, Tetrahedron: Asymmetry **28**, 1304 (2017).
[62] S. Parsons, H.D. Flack, and T. Wagner, Acta Cryst. **B 69**, 249 (2013).
[63] N.K. Hansen and P. Coppens, Acta Cryst. A **34**, 909 (1978).
[64] V. Legrand, S. Pillet, M. Souhassou, N. Lugan, and C. Lecomte, J. Am. Chem. Soc. **128**, 13921 (2006).
[65] S. Pillet, V. Legrand, H.-P. Weber, M. Souhassou, J.-F. Létard, P. Guionneau, and C. Lecomte, Z. Kristallog. **223**, 235 (2008).
[66] H. Romstedt, A. Hauser, and H. Spiering, J. Phys. Chem. Solids **59**, 265 (1998).
[67] K. Boukheddaden, Eur. J. Inorg. Chem. **2013**, 865 (2013).
[68] C.-F. Sheu, S. Pillet, Y.-C. Lin, S.-M. Chen, I.-J. Hsu, C. Lecomte, and Y. Wang, Inorg. Chem. **47**, 10866 (2008).
[69] R. Bertoni, M. Lorenc, H. Cailleau, A. Tissot, J. Laisney, M.-L. Boillot, L. Stoleriu, A. Stancu, C. Enachescu, and E. Collet, Nature Mater. **15**, 606 (2016).
[70] C. Mariette, E. Trzop, S. Zerdane, P. Fertey, D. Zhang, F.J. Valverde-Muñoz, J.-A. Real, and E. Collet, Acta Cryst. B **73**, 660 (2017).
[71] D. Zhang, E. Trzop, F.J. Valverde-Muñoz, L. Piñeiro-López, M.C. Muñoz, E. Collet, and J.A. Real, Crystal Growth & Design **17**, 2736 (2017).
[72] E. Trzop, D. Zhang, L. Piñeiro-Lopez, F.J. Valverde-Muñoz, M. Carmen Muñoz, L. Palatinus, L. Guerin, H. Cailleau, J.A. Real, and E. Collet, Angew. Chem. Int. Ed. **55**, 8675 (2016).
[73] S.M. Neville, B.A. Leita, G.J. Halder, C.J. Kepert, B. Moubaraki, J.-F. Létard, and K.S. Murray, Chem. Eur. J. **14**, 10123 (2008).
[74] J. Kusz, M. Zubko, R.B. Neder, and P. Gütlich, Acta Cryst. B **68**, 40 (2012).
[75] S. Pillet, E.-E. Bendeif, S. Bonnet, H.J. Shepherd, and P. Guionneau, Phys. Rev. B **86**, 064106 (2012).
[76] H. Watanabe, N. Bréfuel, E. Collet, L. Toupet, K. Tanaka, and J.-P. Tuchagues, Eur. J. Inorg. Chem. **2013**, 710 (2013).
[77] J. Cruddas and B.J. Powell, Inorg. Chem. Front. **7**, 4424 (2020).
[78] M. Shatruk, H. Phan, B.A. Chrisostomo, and A. Suleimenova, Coord. Chem. Rev. **289–290**, 62 (2015).
[79] C. Mariette, E. Trzop, J.-Y. Mevellec, A. Boucekkine, A. Ghoufi, G. Maurin, E. Collet, M.C. Muñoz, J.A. Real, and B. Toudic, Phys. Rev. B **101**, 134103 (2020).
[80] N. Brefuel, H. Watanabe, L. Toupet, J. Come, N. Matsumoto, E. Collet, K. Tanaka, and J.-P. Tuchagues, Angew. Chem. Int. Ed. **48**, 9304 (2009).
[81] D. Chernyshov, H.-B. Bürgi, M. Hostettler, and K.W. Törnroos, Phys. Rev. B **70**, 094116 (2004).
[82] M. Nishino, K. Boukheddaden, S. Miyashita, and F. Varret, Phys. Rev. B **68**, 224402 (2003).
[83] A. Bousseksou, F. Varret, and J. Nasser, J. Phys. I France **3**, 1463 (1993).
[84] H. Watanabe, K. Tanaka, N. Bréfuel, H. Cailleau, J.-F. Létard, S. Ravy, P. Fertey, M. Nishino, S. Miyashita, and E. Collet, Phys. Rev. B **93**, 014419 (2016).
[85] K. Boukheddaden, J. Linares, R. Tanasa, and C. Chong, J. Phys.: Condens. Matter **19**, 106201 (2007).
[86] M. Paez-Espejo, M. Sy, and K. Boukheddaden, J. Am. Chem. Soc. **138**, 3202 (2016).
[87] R. Traiche, M. Sy, and K. Boukheddaden, J. Phys. Chem. C 14 (2018).
[88] S. Bonnet, M.A. Siegler, J.S. Costa, G. Molnár, A. Bousseksou, A.L. Spek, P. Gamez, and J. Reedijk, Chem. Commun. 5619 (2008).
[89] V. Heine and J.D.C. McConnell, J. Phys. C: Solid State Phys. **17**, 1199 (1984).
[90] S. Pillet, J. Hubsch, and C. Lecomte, Eur. Phys. J. B **38**, 541 (2004).
[91] K. Ridier, G. Molnár, L. Salmon, W. Nicolazzi, and A. Bousseksou, Solid State Sci. **74**, A1 (2017).
[92] S. Bedoui, G. Molnár, S. Bonnet, C. Quintero, H.J. Shepherd, W. Nicolazzi, L. Salmon, and A. Bousseksou, Chem. Phys. Lett. **499**, 94 (2010).
[93] M. Lopes, C.M. Quintero, E.M. Hernández, V. Velázquez, C. Bartual-Murgui, W. Nicolazzi, L. Salmon, G. Molnár, and A. Bousseksou, Nanoscale **5**, 7762 (2013).
[94] E.K.H. Salje, *Phase Transitions in Ferroelastic and Co-Elastic Crystals: An Introduction for Mineralogists, Material Scientists, and Physicists* (Cambridge University Press, Cambridge [England] ; New York, 1990).

[95] K. Aizu, Phys. Rev. B **2**, 754 (1970).
[96] M.A. Tanatar, A. Kreyssig, S. Nandi, N. Ni, S.L. Bud'ko, P.C. Canfield, A.I. Goldman, and R. Prozorov, Phys. Rev. B **79**, 180508 (2009).
[97] N. Huby, L. Guérin, E. Collet, L. Toupet, J.-C. Ameline, H. Cailleau, T. Roisnel, T. Tayagaki, and K. Tanaka, Phys. Rev. B **69**, 020101 (2004).
[98] A. Goujon, B. Gillon, A. Debede, A. Cousson, A. Gukasov, J. Jeftic, G.J. McIntyre, and F. Varret, Phys. Rev. B **73**, 104413 (2006).
[99] F. Varret, K. Boukheddaden, C. Chong, A. Goujon, B. Gillon, J. Jeftic, and A. Hauser, Europhys. Lett. **77**, 30007 (2007).
[100] F. Varret, C. Chong, A. Goujon, and K. Boukheddaden, J. Phys.: Conf. Ser. **148**, 012036 (2009).
[101] S. Pillet, V. Legrand, M. Souhassou, and C. Lecomte, Phys. Rev. B **74**, 140101 (2006).
[102] M. Buron-Le Cointe, J. Hébert, C. Baldé, N. Moisan, L. Toupet, P. Guionneau, J.F. Létard, E. Freysz, H. Cailleau, and E. Collet, Phys. Rev. B **85**, 064114 (2012).
[103] K. Ichiyanagi, J. Hebert, L. Toupet, H. Cailleau, P. Guionneau, J.-F. Létard, and E. Collet, Phys. Rev. B **73**, 060408 (2006).
[104] M. Avrami, J. Chem. Phys. **7**, 1103 (1939).
[105] M. Avrami, J. Chem. Phys. **8**, 212 (1940).
[106] M. Nishino, K. Boukheddaden, Y. Konishi, and S. Miyashita, Phys. Rev. Lett. **98**, 247203 (2007).
[107] C. Enachescu, L. Stoleriu, A. Stancu, and A. Hauser, Phys. Rev. Lett. **102**, 257204 (2009).
[108] C. Enachescu, M. Nishino, S. Miyashita, A. Hauser, A. Stancu, and L. Stoleriu, Europhys. Lett. **91**, 27003 (2010).
[109] W. Nicolazzi, S. Pillet, and C. Lecomte, Phys. Rev. B **78**, 174401 (2008).
[110] W. Nicolazzi and S. Pillet, Phys. Rev. B **85**, 094101 (2012).
[111] W. Nicolazzi, S. Pillet, and C. Lecomte, Phys. Rev. B **80**, 132102 (2009).
[112] W. Nicolazzi, thèse de l'Université de Lorraine (2008).
[113] J. Sapriel, Phys. Rev. B **12**, 5128 (1975).
[114] V. Janovec, Ferroelectrics **12**, 43 (1976).
[115] M. Sy, F. Varret, K. Boukheddaden, G. Bouchez, J. Marrot, S. Kawata, and S. Kaizaki, Angew. Chem. Int. Ed. **53**, 7539 (2014).
[116] S. Lakhloufi, M.H. Lemée-Cailleau, G. Chastanet, P. Rosa, N. Daro, and P. Guionneau, Phys. Chem. Chem. Phys. **18**, 28307 (2016).
[117] J. Kusz, H. Spiering, and P. Gütlich, J. Appl. Crystallogr. **34**, 229 (2001).
[118] J. Kusz, H. Spiering, and P. Gütlich, J. Appl. Crystallogr. **37**, 589 (2004).
[119] J. Kusz, P. Gütlich, and H. Spiering, in *Spin Crossover in Transition Metal Compounds II* (Springer Berlin Heidelberg, Berlin, Heidelberg, 2004), pp. 129–153.
[120] L. Wiehl, H. Spiering, P. Gütlich, and K. Knorr, J. Appl. Crystallogr. **23**, 151 (1990).
[121] P. Adler, L. Wiehl, E. Meibner, H. Spiering, and P. Gutlich, J. Phys. Chem. Solids **48**, 517 (1987).
[122] M.T.D. Perez, A. Tissot, L. Guénée, A. Hauser, F.J. Valverde-Muñoz, M. Seredyuk, J.A. Real, S. Pillet, E.-E. Bendeif, and C. Besnard, Journal of the American Chemical Society 13 (n.d.).
[123] E. Milin, V. Patinec, S. Triki, E.-E. Bendeif, S. Pillet, M. Marchivie, G. Chastanet, and K. Boukheddaden, Inorg. Chem. **55**, 11652 (2016).
[124] T. Boonprab, S.J. Lee, S.G. Telfer, K.S. Murray, W. Phonsri, G. Chastanet, E. Collet, E. Trzop, G.N.L. Jameson, P. Harding, and D.J. Harding, Angew. Chem. Int. Ed. **58**, 11811 (2019).
[125] C. Enachescu and W. Nicolazzi, C. R. Chim. **21**, 1179 (2018).
[126] G. Lebedev, S. Pillet, C. Baldé, P. Guionneau, C. Desplanches, and J.F. Létard, IOP Conf. Ser.: Mater. Sci. Eng. **5**, 012025 (2009).
[127] T. Delgado, A. Tissot, C. Besnard, L. Guénée, P. Pattison, and A. Hauser, Chem. Eur. J. **21**, 3664 (2015).